



1 Understanding Processes that Control Dust Spatial Distributions with 2 Global Climate Models and Satellite Observations

3 Mingxuan Wu^{1,2}, Xiaohong Liu^{1,3}, Hongbin Yu⁴, Hailong Wang², Yang Shi^{1,3}, Kang Yang⁵, Anton Darmenov⁴,
4 Chenglai Wu¹, Zhien Wang⁵, Tao Luo¹, Yan Feng⁶, Ziming Ke^{1,3}

5 ¹Department of Atmospheric Science, University of Wyoming, Laramie, WY, USA

6 ²Atmospheric Sciences and Global Change Division, Pacific Northwest National Laboratory, Richland, WA,
7 USA

8 ³Department of Atmospheric Sciences, Texas A&M University, College Station, Texas, USA

9 ⁴NASA Goddard Space Flight Center, Greenbelt, Maryland, USA

10 ⁵Department of Atmospheric and Oceanic Sciences, University of Colorado Boulder, Boulder, CO, USA

11 ⁶Environmental Science Division, Argonne National Laboratory, Argonne, IL, USA

12 *Correspondence to:* Xiaohong Liu (xiaohong.liu@tamu.edu)

13 Abstract

14 Dust aerosol is important in modulating the climate system at local and global scales, yet its spatiotemporal
15 distributions simulated by global climate models (GCMs) are highly uncertain. In this study, we evaluate the
16 spatiotemporal variations of dust extinction profiles and dust optical depth (DOD) simulated by the
17 Community Earth System Model version 1 (CESM1) and version 2 (CESM2), the Energy Exascale Earth
18 System Model version 1 (E3SMv1), and the Modern-Era Retrospective analysis for Research and
19 Applications version 2 (MERRA-2) against satellite retrievals from Cloud-Aerosol Lidar with Orthogonal
20 Polarization (CALIOP), Moderate Resolution Imaging Spectroradiometer (MODIS), and Multi-angle
21 Imaging SpectroRadiometer (MISR). We find that CESM1, CESM2, and E3SMv1 underestimate dust
22 transport to remote regions. E3SMv1 performs better than CESM1 and CESM2 in simulating dust transport
23 and the northern hemispheric DOD due to its higher mass fraction of fine dust. CESM2 performs the worst
24 in the northern hemisphere due to its lower dust emission than in the other two models but has a better dust
25 simulation over the Southern Ocean due to the overestimation of dust emission in the southern hemisphere.
26 DOD from MERRA-2 agrees well with CALIOP DOD in remote regions due to its higher mass fraction of



27 fine dust and the assimilation of aerosol optical depth. The large disagreements in the dust extinction profiles
28 and DOD among CALIOP, MODIS, and MISR retrievals make the model evaluation of dust spatial
29 distributions challenging. Our study indicates the importance of representing dust emission, dry/wet
30 deposition, and size distribution in GCMs in correctly simulating dust spatiotemporal distributions.

31

32 **1 Introduction**

33 Mineral dust plays an important role in the Earth's climate system. It can impact the Earth's radiation
34 budget directly through scattering and absorbing solar and terrestrial radiation (e.g., Tegen et al., 1996;
35 Balkanski et al., 2007), and indirectly through acting as cloud condensation nuclei and ice nucleating particles
36 (e.g., Rosenfeld et al., 2001; DeMott et al., 2003; Shi and Liu, 2019). Dust can reduce the snow albedo when
37 deposited on snow (e.g., Yasunari et al., 2015; Wu et al., 2018b; Rahimi et al., 2019), participate in the
38 heterogeneous atmospheric chemistry reactions (e.g., Dentener et al., 1996), and provide nutrients such as
39 iron to oceans through deposition (e.g., Jickells et al., 2005). Dust aerosols are reported to have a negative
40 radiative forcing (RF) due to aerosol-radiation interactions (RF_{ari}); however, large uncertainties exist in the
41 dust RF_{ari} estimates (Boucher et al., 2013). Whether mineral dust warms or cools the climate is still
42 controversial (e.g., Boucher et al., 2013; Scanza et al., 2015; Kok et al., 2017).

43 The large uncertainties in estimating dust RF_{ari} can be mainly attributed to the large diversities in the
44 dust lifecycle (i.e., emission, transport and deposition) simulated by current global climate models (GCMs)
45 (e.g., Huneus et al., 2011; Boucher et al., 2013; Kim et al., 2014, 2019; Pu & Ginoux, 2018; Wu et al.,
46 2018a), which is not well constrained by observations. Huneus et al. (2011) found that global total dust
47 emission from 14 GCMs participating in the Aerosol Comparisons between Observations and Models
48 (AeroCom) Phase I ranges from 514 to 4313 Tg yr⁻¹ while global annual mean dust optical depth (DOD)



49 ranges from 0.010 to 0.053. Pu and Ginoux (2018) showed that the Coupled Model Intercomparison Project
50 Phase 5 (CMIP5) models underestimate DOD, especially in spring, compared with land DOD derived from
51 MODIS. Wu et al. (2018a) found that dust emission from CMIP5 models differs greatly in spatial distribution
52 and intensity over East Asia. Kim et al. (2014, 2019) compared DOD from 5 GCMs participating in the
53 AeroCom Phase II with DOD derived from the Cloud-Aerosol Lidar with Orthogonal Polarization (CALIOP),
54 Moderate Resolution Imaging Spectroradiometer (MODIS), and Multiangle Imaging Spectroradiometer
55 (MISR) in the trans-Atlantic and trans-Pacific regions, respectively. Large diversities are found in the
56 modeled DOD over the source regions of North Africa and East Asia, implying large uncertainties associated
57 with dust emissions in these models. The low model biases of DOD across the North Atlantic and North
58 Pacific indicate that current GCMs underestimate the trans-Atlantic transport of North African dust and the
59 trans-Pacific transport of East Asian dust, respectively, likely due to an overestimation of dust removal.

60 Apart from horizontal distribution, the vertical distribution of mineral dust can strongly influence the
61 radiative effects of dust (e.g., Zhang et al., 2013), which is poorly constrained by observations. Few studies
62 directly compared dust extinction profiles in GCMs with retrievals from CALIOP onboard Cloud-Aerosol
63 Lidar and Infrared Pathfinder Satellite Observation (CALIPSO) (e.g., Yu et al. 2010; Johnson et al., 2012;
64 Kim et al., 2019; Wu et al., 2019). Yu et al. (2010) separated the dust extinction from the total aerosol
65 extinction in the nighttime cloud-free CALIOP level 2 (CAL-L2) version 2.01 product using the volume
66 depolarization ratio. They compared the dust extinction simulated by the Goddard Chemistry Aerosol
67 Radiation Transport (GOCART) model with CALIPSO observations from June 2006 to November 2007.
68 Johnson et al. (2012) evaluated the dust extinction simulated by GEOS-Chem, a global 3-D chemical
69 transport model driven by meteorological input from the Goddard Earth Observing System (GEOS), with
70 CAL-L2 version 3.01 product from March 2009 to February 2010 and found high model biases of dust



71 extinction in the lower troposphere over main source regions, similar as Yu et al. (2010). Wu et al. (2019)
72 compared dust extinction modeled by the Community Earth System Model (CESM) with satellite retrievals
73 from Luo et al. (2015a, 2015b) (L15), Yu et al. (2015) (Y15), and standard CALIOP level 3 (CAL-L3) product
74 and found high model biases of dust extinction in the upper troposphere and large uncertainties in different
75 CALIPSO products over East Asia.

76 A major challenge in evaluating mineral dust in GCMs is the lack of high-quality and long-term
77 measurements of dust (Evan et al., 2014). The limited spatiotemporal coverage of ground-based and aircraft
78 observations is insufficient to provide global scale dust information. Pu and Ginoux (2016) derived DOD
79 over land from MODIS Deep Blue aerosol products using Ångström exponent and single scattering albedo.
80 Compared to coarse mode aerosol optical depth (AOD) from Aerosol Robotic Network (AERONET) ground-
81 based observations, MODIS DOD over land is slightly underestimated. Yu et al. (2009) derived DOD over
82 ocean from MODIS Dark Target aerosol products using prescribed fine mode fractions of combustion, dust,
83 and marine aerosols. MODIS DOD over ocean shows that Asian dust can contribute substantially to the
84 aerosol loading over North America (Yu et al., 2012). Luo et al. (2015a) developed a dust separation method
85 to retrieve dust extinction from CAL-L1B product, which gives lower dust extinction in the lower troposphere
86 (< 4 km) than CAL-L2 product. Luo et al. (2015b) developed a dust identification method to better detect
87 optically thin dust layers and found significantly frequent dust occurrences in the upper troposphere than
88 CAL-L2 product. Ridley et al. (2016) estimated the global DOD to be 0.030 ± 0.005 by combining satellite
89 retrievals of AOD with DOD simulated by four global models, which is close to AeroCom mean ($0.028 \pm$
90 0.011 , Huneus et al., 2011) but has less uncertainties.

91 In this study, we compare dust extinction profiles and DOD simulated from CESM1, CESM2, the Energy
92 Exascale Earth System Model version 1 (E3SMv1) and the Modern-Era Retrospective analysis for Research



93 and Applications version 2 (MERRA-2) with satellite retrievals from CALIOP (L15 and Y15), MODIS, and
94 MISR on a global scale. We pay attention not only to the physical processes responsible for the model biases
95 of dust but also to the uncertainties in satellite retrievals and the impacts of these uncertainties on the model
96 evaluation. The goal of this study is to evaluate the performance of CESM1, CESM2, E3SMv1, and MERRA-
97 2 in the simulations of (1) dust mass budgets, (2) dust extinction profiles and DOD, and (3) dust surface
98 concentrations. The paper is organized as follows. Section 2 first introduces the models (CESM1, CESM2,
99 E3SMv1, and MERRA-2), and then gives a detailed description of the satellite retrievals used in this study.
100 Section 3 first shows the global dust mass budgets from the four models and then compares modeled dust
101 extinction profiles and DOD with satellite retrievals. Discussion and conclusions are presented in section 4.

102

103 **2 Models and Data**

104 In this section, we give a brief description of the GCMs (Section 2.1), experiments design (Section 2.2),
105 and satellite retrievals (Section 2.3) used in this study. Some important model features for simulating dust in
106 CESM1, CESM2, E3SMv1, and MERRA-2 are summarized in Table 1.

107

108 **2.1 Model Description**

109 **2.1.1 CESM**

110 In this study, we use the latest CESM2.1 with the Community Atmosphere Model version 6 (CAM6) and
111 the Community Land Model version 5 (CLM5, Lawrence et al., 2019) as the atmosphere and land component,
112 respectively. CAM6 has replaced earlier schemes for boundary layer turbulence, shallow convection and
113 cloud macrophysics with the Cloud Layers Unified by Binormals (CLUBB, Golaz et al., 2002; Bogenschutz
114 et al., 2013) scheme. CAM6 uses an improved two-moment cloud microphysics (MG2, Gettelman and



115 Morrison, 2015) scheme and the four-mode version of Modal Aerosol Module (MAM4, Liu et al., 2016).
116 Dust is represented in the Aitken mode, accumulation mode, and coarse mode with emission diameter bounds
117 at 0.01-0.1 μm , 0.1-1.0 μm , and 1.0-10.0 μm , respectively. Dust emission is parameterized following Zender
118 et al. (2003a). A geomorphic source function is used to account for global variations in soil erodibility, which
119 is proportional to the upstream runoff collection area (Zender et al., 2003b). The size distribution of emitted
120 dust particles follows the brittle fragmentation theory (Kok, 2011) with prescribed mass fractions of
121 0.00165%, 1.1%, and 98.9% for the three modes, respectively.

122 For comparison, we also use CESM1.2 (Hurrell et al., 2013) with CAM5 (Neale et al., 2010) and CLM4
123 (Oleson et al., 2010) as the atmosphere and land component, respectively. As shown in Table 1, the
124 representation of dust in aerosol module, dust emission scheme, and size distribution in CESM2.1 is the same
125 as in CESM1.2. The main difference of dust treatment is that CESM2.1 reduces the geometric standard
126 deviations in the accumulation and coarse mode, from 1.8 to 1.6 and 1.2, respectively. This greatly reduces
127 the dry deposition velocities for dust particles in the accumulation and coarse mode, which further leads to
128 the decrease of dust dry deposition fluxes. The geomorphic source function used in CESM2.1 is also different
129 from the one used in CESM1.2 (see Fig. S1), which substantially changes the spatial distributions of dust
130 emission.

131

132 **2.1.2 E3SM**

133 We use E3SMv1 (Golaz et al., 2019) with the atmosphere model (EAM, Rasch et al., 2019) and land
134 model (ELM), which are based on CAM5 and CLM4.5, respectively, as the atmosphere and land component.
135 Compared with CAM6, EAMv1 includes new treatments of convective transport, wet removal, and
136 resuspension of aerosols to the coarse mode (Wang et al., 2013, 2020), which can reduce the high model



137 biases of dust extinction in the upper troposphere. Dust is carried in the accumulation and coarse mode with
138 emission diameter bounds at 0.1-1.0 μm , and 1.0-10.0 μm , respectively. Unlike CESM1.2 and CESM2.1, the
139 size distribution of emitted dust particles follows Zender et al. (2003a) with prescribed mass fractions of 3.2%
140 and 96.8% for the accumulation and coarse mode, respectively (see Table 1). The higher mass fraction of
141 emitted accumulation mode dust in E3SMv1, which is three times larger than that in CESM2.1, can increase
142 the dust transport to remote regions (e.g., Arctic, Antarctic, and Southern Ocean). However, it overestimates
143 the mass fraction of emitted fine dust compared with observations, as shown in Kok (2011). E3SMv1 uses
144 the same source function as CESM1.2 for dust emission, indicating that E3SMv1 has similar spatial
145 distributions of dust emission to CESM1.2. Compared with CESM1.2 and CESM2.1, E3SMv1 has 72 vertical
146 layers and its bottom layer thinner than that in CESM1.2 and CESM2.1, which can affect the dry deposition
147 of dust.

148

149 **2.1.3 MERRA-2**

150 MERRA-2 (Gelaro et al., 2017) is the latest atmospheric reanalysis of the modern satellite era produced
151 by combining GEOS atmospheric model version 5 (GEOS-5) with a 3D variational data assimilation
152 (3DVAR) algorithm to ingest a wide range of observational data. MERRA-2 assimilates AOD from the
153 Advanced Very High Resolution Radiometer (AVHRR), MODIS, MISR, and AERONET. GEOS-5 is run
154 with GOCART aerosol module (Chin et al., 2002). The dust emission flux is calculated based on Ginoux et
155 al. (2001). A topographic source function (see Fig. S1) is used to shift dust emission towards the most erodible
156 regions, which is characterized by the relative elevation of source regions in surrounding basins (Ginoux et
157 al., 2001). We should note that the assimilation of AOD results in the imbalance of global dust mass. Because
158 the assimilation of AOD increases dust concentrations in remote regions, the total deposition (dry and wet)



159 is considerably larger than the dust emission in MERRA-2. As shown in Table 1, dust is carried in 5 size bins
160 with diameter bounds at 0.2-2.0 μm , 2.0-3.6 μm , 3.6-6.0 μm , 6.0-12.0 μm , and 12.0-20.0 μm , respectively.
161 The size distribution of emitted dust particles follows Tegen and Lacis (1996) with mass fractions of 6.6%,
162 20.6%, 22.8%, 24.5%, and 25.4%, respectively. MERRA-2 includes very coarse dust (10.0-20.0 μm), which
163 is neglected by CESM and E3SM. MERRA-2 also has the highest mass fraction of emitted fine dust (0.1-10
164 μm) among the four models (see Figure 3 in Kok 2011), which can increase the dust transport.

165

166 **2.2 Experiments Design**

167 We ran CESM1.2 and CESM2.1 with the finite-volume (FV) dynamical core for CAM5.3 and CAM6,
168 respectively, at $0.9^\circ \times 1.25^\circ$ horizontal resolution with 56 vertical levels from 2006 to 2009, and the last 3-
169 year results were used for analysis. We ran E3SMv1 with the spectral-element (SE) dynamical core for
170 EAMv1 at 100 km horizontal resolution on a cubed-sphere geometry with 72 vertical layers from 2006 to
171 2009. The horizontal wind components u and v were nudged towards the MERRA-2 meteorology using a
172 relaxation time scale of 6 hours. Monthly mean climatological SST and sea ice concentrations were used.
173 The dust emission in CESM1.2, CESM2.1, and E3SMv1 was tuned so that AOD in the dusty region
174 ($\text{DOD}/\text{AOD} > 0.5$) matches observations from MODIS onboard Terra and Aqua.

175

176 **2.3 Satellite Retrievals**

177 **2.3.1 MODIS and MISR**

178 Pu and Ginoux (2016) derived DOD over land from MODIS Collection 6 (C6) Deep Blue aerosol
179 products (Hsu et al., 2013) by using a continuous function relating the Ångström exponent (α) to fine mode
180 AOD established by Anderson et al. (2005) which was derived based on ground measurements. The formula



181 is given as:

$$182 \quad DOD = AOD \times (0.98 - 0.5089\alpha + 0.0512\alpha^2) \quad (\alpha < 0.3, \omega < 1) \quad (1)$$

183 where ω is the single scattering albedo at 470 nm. DOD is derived only when α is less than 0.3 and ω is less
184 than 1. As discussed in Baddock et al. (2016), we use the lowest quality (QA=1) AOD over dust source
185 regions and AOD flagged as very good quality (QA=3) for other land areas. Although the derived MODIS
186 DOD over land is in good agreement with coarse mode AOD from AERONET (Pu and Ginoux, 2016), it
187 may overestimate DOD in reality. We calculate coarse mode AOD, which is used as a proxy of DOD, only
188 when AOD is mainly contributed by dust ($\alpha < 0.3, \omega < 1$).

189 Yu et al. (2019) derived DOD over ocean from MODIS C6 Dark Target aerosol products as follows:

$$190 \quad DOD = \frac{AOD(f_c - f) - AOD_m(f_c - f_m)}{(f_c - f_d)} \quad (2)$$

191 where f is the fine mode fraction retrieved directly from MODIS; AOD_m is the marine AOD; f_c, f_d , and f_m are
192 fine mode fractions of combustion, dust, and marine aerosol, respectively. F_c, f_d , and f_m are set to be 0.92
193 (0.89), 0.26 (0.31), and 0.55 (0.48) for MODIS onboard Terra (Aqua), respectively. These differences in the
194 fractions may be caused by the difference in instrument calibrations (Levy et al., 2018). We also use the
195 nonspherical fraction of AOD from MISR (Witek et al., 2018) as a proxy of DOD over ocean (e.g., Kim et
196 al., 2014, 2019; Yu et al., 2019). We do not use MODIS and MISR DOD over high-latitude regions ($> 60^\circ$)
197 because of large uncertainties in retrievals.

198

199 2.3.2 CALIOP

200 Luo et al. (2015a) developed a new dust separation method which derives the dust backscatter coefficient
201 ($\beta_d, \text{m}^{-1} \text{sr}^{-1}$) in the lidar equation inversion stage using the CAL-L1B data. The original single-scattering
202 lidar equation is:



203
$$\beta'(z) = (\beta_a(z) + \beta_m(z))e^{-2 \int_0^z (S_a \beta_a(z') + S_m \beta_m(z')) dz'} \quad (3)$$

204 where β' (CAL-L1B product) is the total attenuated backscatter coefficient; β_a (CAL-L2 product) and β_m are
205 backscatter coefficients for aerosol and molecules, respectively; S_a and S_m are lidar ratios for aerosol and
206 molecules, respectively. Assuming that dust is externally mixed with non-dust aerosols, Eq. (3) can be
207 rewritten as:

208
$$\beta'(z) = (\beta_a(z) + \beta_{nd}(z) + \beta_m(z))e^{-2 \int_0^z (S_d \beta_d(z') + S_{nd} \beta_{nd}(z') + S_m \beta_m(z')) dz'} \quad (4)$$

209 where β_d and β_{nd} are backscatter coefficients for dust and non-dust aerosols, respectively; S_d is the lidar ratio
210 for dust and set to be 40 sr; S_{nd} is the lidar ratio for non-dust aerosols and set to be 25 sr. The new separation
211 method also requires a priori knowledge of depolarization ratios of dust (δ_d) and non-dust (δ_{nd}), which are
212 given values of 0.25 and 0.05, respectively. The dust extinction can then be easily converted from β_d by
213 multiplying S_d of 55 sr, which accounts for the multiple scattering effects as suggested in Wandinger et al.
214 (2010). The new separation method can resolve dust extinction from polluted dust (i.e. dust mixing with other
215 types of aerosols), whereas CAL-L2 products fail to do so. It also tends to have less uncertainties than doing
216 the partition based on lidar inversion products (i.e., CAL-L2) in previous studies (e.g., Amiridis et al., 2013;
217 Proestakis et al., 2018; Yu et al., 2015). Additionally, Luo et al. (2015b) developed a new dust identification
218 method by using combined lidar-radar cloud masks from CloudSat and CALIPSO, which significantly
219 improves the detection of optically thin dust layer, especially in the upper troposphere. In this study, we use
220 both the new separation method (Luo et al., 2015a) and the new identification method (Luo et al., 2015b) to
221 produce the nighttime dust extinction dataset (L15) for the period of 2007 to 2009.

222 Yu et al. (2015) derived β_d from CAL-L2 β_a with a priori knowledge of δ_d and δ_{nd} as follows:

223
$$\beta_d = \frac{(\delta - \delta_{nd})(1 + \delta_a)}{(1 + \delta)(\delta_a - \delta_{nd})} \beta_a \quad (5)$$

224 where δ is the CALIOP observed particulate depolarization ratio. To minimize the uncertainties, we calculate



225 β_d in two scenarios: the “lower-bound dust fraction” scenario ($\delta_d=0.30$, $\delta_{nd}=0.07$) and the “upper-bound dust
226 fraction” scenario ($\delta_d=0.20$, $\delta_{nd}=0.02$). We then converted dust extinction from β_d by multiplying S_d of 45 sr.
227 In this study, we use the dust separation method to retrieve nighttime dust extinction under the cloud free
228 condition based on CAL-L2 version 4 lidar products. To ensure the retrieval quality, we only select high-
229 confidence data based on the cloud-aerosol discrimination (CAD) scores (-100 to -70) and extinction quality
230 control flag values (0, 1, 16, and 18) (Yu et al., 2010; Yu et al., 2015). The aerosol free condition (dust
231 extinction is zero) is also included in the retrieval.

232 To make an apple-to-apple comparison of modeled dust extinction with satellite observations, two
233 treatments were applied to collocate model results and CALIOP data. First, dust extinction retrievals from
234 L15 and Y15 were averaged into $0.9^\circ \times 1.25^\circ$ grid boxes (same as CAM5.3 and CAM6) and interpolated to
235 pressure levels at 25 hPa intervals. Modeled dust extinction profiles from CESM1.2, CESM2.1, and E3SMv1
236 were sampled every 10 s along the CALIPSO satellite tracks. Dust extinction profiles from MERRA-2 were
237 calculated offline based on 3-hourly output of 3-D dust mixing ratio and then sampled along the CALIPSO
238 satellite tracks. Second, the dust extinction in and below the vertical layer where cloud fraction is 100% was
239 set to missing values to account for the fact that dust inside clouds, adjacent to the cloud bottom, and below
240 optically thick clouds cannot be retrieved from CALIOP. Collocated dust extinction from model experiments
241 is then integrated vertically to get the DOD value.

242

243 **3 Results**

244 Figure 1a shows 12 selected regions including both dust source regions and transport pathway regions,
245 in which we evaluate the seasonal variations of modeled dust extinction and DOD with satellite retrievals.
246 Figure 1b shows the network of stations, at which we evaluate dust surface concentrations (Huneeus et al.,



247 2011; Prospero et al., 2012; Fan, 2013).

248

249 **3.1 Dust Mass Budgets**

250 Table 2 gives the global annual mean dust mass budgets, DOD, and mass extinction efficiency (MEE)
251 from model experiments. We can see that dust emissions in CESM1 and E3SMv1 are much larger than those
252 in CESM2 and MERRA-2, which can be attributed to the model tuning and uses of different dust emission
253 schemes and source functions. Dust emission schemes in CESM1, CESM2, and E3SMv1 are the same and
254 based on Zender et al. (2003a), while dust emission scheme in MERRA-2 is based on Ginoux et al. (2001).
255 CESM1 and E3SMv1 use the same dust source function which is different from those in CESM2 and
256 MERRA-2. Dry deposition is the dominant removal process of dust compared with wet deposition in CESM1,
257 E3SMv1, and MERRA-2, whereas CESM2 has less dry deposition (675 Tg yr^{-1}) than wet deposition (1151
258 Tg yr^{-1}). Due to the decrease of geometric standard deviations in the accumulation and coarse mode of
259 CESM2 MAM4 (see Table 1), aerosol dry deposition velocities for the accumulation and coarse mode greatly
260 reduce, leading to the decrease of dry deposition. Note that MERRA-2 has less dry deposition (750 Tg yr^{-1})
261 than wet deposition (865 Tg yr^{-1}) for dust aerosols with diameter between 0.2 and $12.0 \mu\text{m}$. We also find that
262 E3SMv1 produces notably higher dry deposition than CESM1, although both models have similar amount of
263 dust emission. In CESM and E3SM, dust emission fluxes ($\text{kg m}^{-2} \text{ s}^{-1}$) are divided by the model bottom layer
264 thickness and converted to dust mixing ratio tendencies ($\text{kg kg}^{-1} \text{ s}^{-1}$). Because the bottom layer in E3SMv1
265 is thinner with higher vertical resolution than the one in CESM1, more dust in the bottom layer is removed
266 through dry deposition process.

267 As CESM2 has much less dust dry deposition than wet deposition, larger fraction of dust is transported
268 away from the major source regions in CESM2 than CESM1. Dust lifetime in CESM2 (3.90 days) is longer



269 than that in CESM1 (2.33 days). E3SMv1 has a smaller dust burden and a shorter lifetime but larger DOD
270 than CESM1 due to the larger dry deposition and higher mass fraction of dust in the accumulation mode,
271 respectively. Since MERRA-2 has the largest mass fraction of fine dust among the four models and
272 assimilates AOD, dust in MERRA-2 has the longest lifetime (4.19 days) and largest global mean DOD
273 (0.0312), despite its lowest dust emission. Note that MERRA-2 has considerably larger dust deposition (dry
274 and wet, 2048 Tg yr⁻¹) than dust emission (1636 Tg yr⁻¹), which is significantly imbalanced, due to the
275 assimilation of AOD. In remote regions where AOD is underestimated, the assimilation of AOD increases
276 dust concentrations resulting in the increase of dust deposition. MEE (DOD/dust burden) is often used for
277 converting dust mass to DOD. As shown in Table 2, it varies from 0.452 (CESM1) to 0.677 m² g⁻¹ (MERRA-
278 2). In Huneus et al. (2011), MEE from AeroCom Phase I models varies from 0.25 to 1.28 m² g⁻¹. Haywood
279 et al. (2003) measured MEE of 0.37 m² g⁻¹ (0.32-0.43 m² g⁻¹) based on aircraft campaigns, which is used in
280 many studies (e.g., Kaufman et al., 2005; Yu et al., 2015). Pu and Ginoux (2018) used a MEE of 0.6 m² g⁻¹
281 to convert dust burden simulated by CMIP5 models to DOD.

282 Figure 2 shows the spatial distributions of global annual mean dust emissions from the model experiments.
283 We can see that CESM1 (Fig. 2a) has similar spatial distributions of dust emission as E3SMv1 (Fig. 2c) due
284 to the use of the same source function and dust emission scheme. Dust emission in MERRA-2 (Fig. 2d)
285 spreads more uniformly than that in CESM1 and E3SMv1, while CESM2 (Fig. 2b) has smaller areas emitting
286 mineral dust than CESM1 and E3SMv1. CESM2 has lower dust emission in main source regions, such as
287 North Africa, Middle East, and East Asia, but has much higher dust emission in South America, South Africa,
288 and Australia than CESM1, E3SMv1, and E3SMv1.

289 Figure 3 shows the seasonal variations of dust emissions from model experiments in six source regions
290 (Fig. 1a). In North Africa (Fig. 3a), CESM1 has the largest dust emission (5000-10000 kt d⁻¹) with the



291 strongest seasonality, while CESM2 has the lowest dust emission (~ 2000 kt d^{-1}). Dust emissions in CESM1,
292 CESM2, E3SMv1, and MERRA-2 peak in April, February, February, and July, respectively. Although
293 CESM1 and E3SMv1 use the same source function and dust emissions scheme, E3SMv1 produces
294 considerably lower dust emission than CESM1. The different height of bottom layer with horizontal wind
295 nudged toward MERRA-2 may cause the differences in friction velocities. Large differences of dust emission
296 can also be found in Northwest China (Fig. 3b). However, dust emissions in the four models have similar
297 seasonality and all peak in May. E3SMv1 produces slightly higher dust emission than CESM1, especially
298 from September to January. CESM1, CESM2, and MERRA-2 produces similar low dust emissions in
299 December and January. In North America (Fig. 3d), CESM2 produces the lowest dust emission with the
300 weakest seasonality among the four models. In the Southern Hemisphere (SH) source regions (Fig. 3c, e and
301 f), CESM2 produces much larger dust emissions than CESM1, E3SMv1, and MERRA-2. In South America,
302 the seasonality of dust emission in CESM2 is significantly different from those in other models, which results
303 from the different location of dust emission (see Fig. 2).

304 Figure 4 shows the seasonal variations of dust burdens from model experiments in the twelve selected
305 regions marked in Fig. 1a. In North Africa (Fig. 4a), CESM1 has the highest dust burden while CESM2 has
306 the lowest dust burden. Although MERRA-2 produces much lower dust emission than E3SMv1, dust burden
307 in MERRA-2 is larger than that in E3SMv1 due to a higher mass fraction of fine dust. Because the
308 assimilation of AOD increases the dust concentrations on the trans-Atlantic pathway, MERRA-2 has the
309 highest dust burden among the four models across the Atlantic (Fig. 4e). In North America (Fig. 4i), dust
310 burden in MERRA-2 is much larger than those in other models, whereas dust emission in MERRA-2 is
311 similar to those in CESM1 and E3SMv1. This is due to the enhanced dust transport over the Pacific, which
312 is further caused by the assimilation of AOD over the Pacific (see Fig. 4f and j). We can see that CESM2



313 produces the highest dust burden with the strongest seasonality in SH source regions (Fig. 4c, g, and k) due
314 to its large dust emission. MERRA-2 has similar dust burden in the Arctic (Fig. 4d) as in Northwest China,
315 indicating that MERRA-2 may overestimate dust burden in the Arctic.

316

317 **3.2 Dust Optical Depth**

318 Figure 5 compares the spatial distributions of modeled DOD with satellite retrievals from CALIOP (82°S-
319 82°N), MODIS (60°S-60°N) and MISR (ocean, 60°S-60°N). The annual mean values are averaged between
320 60°S and 60°N for a better comparison. In general, CESM1, CESM2, and E3SMv1 underestimate global
321 mean DOD compared with CALIOP (L15 and Y15) and MODIS; DOD in MERRA-2 is higher than CALIOP
322 but is still much lower than MODIS DOD. CESM1 overestimate the land DOD (0.0678) compared with
323 observations from L15 (0.0614) and Y15(0.0625); DOD over land in E3SMv1 (0.0615) is between L15 and
324 Y15. However, modeled DOD over ocean in CESM1 (0.0074), CESM2 (0.0087), and E3SMv1 (0.0094) is
325 much lower than retrievals from L15 (0.0137) and Y15 (0.0181), which mainly contributes to the low model
326 biases of global mean DOD. This indicates that CESM1, CESM2, and E3SMv1 underestimate dust transport
327 to remote regions (e.g., Arctic and Southern Ocean). In the Northern Hemisphere (NH), CESM2 produces
328 the lowest DOD over major source regions such as North Africa, Middle East, and East Asia among the four
329 models due to its low dust emission. Since E3SMv1 has higher mass fraction (3.2%) of accumulation mode
330 dust than CESM1 and CESM2 (1.1%), it performs better than CESM1 and CESM2 and simulates more dust
331 transport to the Arctic. In SH, CESM2 produces much larger DOD in South America, South Africa, and
332 Australia than CALIOP due to high dust emission in these three source regions (see Fig. 3), which also leads
333 to a higher DOD over the Southern Ocean than other models and improves the agreement with observations.
334 MERRA-2 tends to have the best agreement with CALIOP in DOD, especially in remote regions, which can



335 be attributed to the assimilation of AOD from satellites and ground-based measurements and high mass
336 fraction of emitted fine dust.

337 Comparing to the DOD estimates from AeroCom models (0.028 ± 0.011 , Huneus et al., 2011) and Ridley
338 et al. (2016) (0.030 ± 0.005), global mean DOD in MERRA-2 and Y15 is close to the global mean value from
339 Ridley et al. (2016); DOD from model experiments is within the uncertainty range of AeroCom models.
340 MODIS DOD (> 0.06) is substantially larger than CALIOP DOD (< 0.03). MISR DOD over ocean is between
341 CALIOP and MODIS DOD. Large uncertainties also exist in DOD retrievals from different sensors, which
342 can affect the model evaluation. The DOD differences between MODIS and CALIOP can come from two
343 main aspects: (1) the differences between AOD retrieved from MODIS and CALIOP and (2) the differences
344 of retrieval algorithms in separating DOD from AOD. Ma et al. (2013) compared CAL-L3 AOD with MODIS
345 AOD from 2006 to 2011 and found that CAL-L3 AOD is lower than MODIS AOD. Global annual mean
346 AOD from nighttime CAL-L3 over ocean is 0.089, while MODIS AOD over ocean is 0.148 and 0.140 for
347 Terra and Aqua, respectively. Ma et al. (2013) also showed that CAL-L3 has lower AOD than MODIS over
348 major dust source regions.

349 MODIS DOD is subject to cloud contamination that can cause a high bias in DOD (e.g., Zhang et al.,
350 2005). In Fig. 5g and h, we can see the apparent discontinuity along the tropical African coast, because
351 MODIS DOD is derived from Deep Blue and Dark Target products over land and ocean, respectively. In
352 addition, MODIS DOD derived from Dark Target products over the turbid-water coastal region is subject to
353 high bias due to the underestimation of surface reflectance. Since Eq. (1) is used to calculate the coarse mode
354 AOD in Anderson et al. (2005) and we derived DOD only when AOD is mainly contributed by dust ($\alpha < 0.3$,
355 $\omega < 1$), MODIS DOD over land may be subject to high bias. Unlike passive sensors, CALIOP may do a better
356 job in discriminating dust from clouds and other types of aerosols and providing the vertical distributions of



357 dust. However, CALIOP cannot penetrate optically thick cloud layers due to strong attenuation of the signals,
358 missing the lowest part of aerosol plumes. CALIOP also fails to detect tenuous dust layers due to weak signals.
359 Notable differences are found between MODIS DOD from Terra (0.0686) and Aqua (0.0615) as well, which
360 can be attributed to the calibration issues of MODIS Terra (e.g., Levy et al., 2018). Ma and Yu (2015) showed
361 that MISR AOD over ocean (0.157) is higher than MODIS Aqua AOD over ocean (0.139). MISR DOD over
362 ocean, especially over the Southern Ocean, may be biased high due to artifacts (e.g., Witek et al., 2013). In
363 this study, we use the latest version (V23) of MISR aerosol products, which significantly reduces AOD over
364 ocean compared to the previous V22 products.

365 Table 3 gives the global seasonal mean DOD (averaged over 60°S-60°N) from model experiments and
366 satellite observations. CESM1, CESM2, and E3SMv1 underestimate global mean DOD in all seasons
367 compared with MODIS and CALIOP, which is mainly attributed to the low model biases of DOD over ocean.
368 DOD from model experiments, Y15, and Terra MODIS all peaks in MAM (March-April-May) and reaches
369 its minimum in DJF (December-January-February) due to the seasonal variations of global dust emission.
370 However, DOD from L15 and Aqua MODIS slightly increases from MAM to JJA (June-July-August) and
371 peaks in JJA. Notable decreases of DOD from MAM to JJA are found in model experiments. The decrease
372 ranges from 0.0012 (E3SMv1) to 0.0096 (MERRA-2), while DOD from Terra MODIS and Y15 slightly
373 decreases by 0.0008 and 0.0019, respectively. Unlike observations and other models, DOD from CESM2
374 increases from JJA to SON (September-October-November) which can be attributed to the overestimation of
375 dust emission in SH. CESM2 also has the weakest seasonal contrast, and the DOD difference between MAM
376 and DJF is only 0.0067. MERRA-2 has the strongest seasonal contrast, and the DOD difference between
377 MAM and DJF is 0.0244.

378 We further examine the dust transport across the Atlantic (0°-35°N) and Pacific (30°N-60°N) by



379 comparing the meridional means of modeled DOD with satellite retrievals from CALIOP, MODIS (combined
380 Terra and Aqua), and MISR, as shown in Fig. 6. In Fig. 6a, satellite retrievals of DOD show high values in
381 North Africa (15°W - 30°E). As dust is transported from North Africa to the Atlantic, DOD gradually decreases.
382 In the source regions, MODIS and CALIOP DOD all peaks between 5°W and 5°E , whereas DOD from
383 CESM1, CESM2, and E3SMv1 peaks in Northeast Africa (30°E) determined by the geomorphic source
384 function used in the models. Although MERRA-2 well captures the meridional variations of DOD due to the
385 use of a topographic source function, it overestimates the DOD compared with CALIOP. This may be caused
386 by the contribution of very coarse dust (10 - $20\ \mu\text{m}$) and high mass fraction of fine dust (0.1 - $1\ \mu\text{m}$). DOD in
387 E3SMv1 agrees the best with CALIOP DOD among the four models. CESM1 produces substantially larger
388 DOD (0.25 - 0.38) in Northeast Africa (15°E - 30°E) than CALIOP but agrees well with CALIOP in Northwest
389 Africa (15°W - 5°E). CESM2 significantly underestimates DOD (~ 0.1) in Northwest Africa (15°W - 5°E)
390 compared with CALIOP due to its underestimation of dust emission (see Fig. 3a).

391 Over the entire Atlantic, modeled DOD in CESM1, CESM2, and E3SMv1 is lower than observations,
392 which may result from the fast deposition and short lifetime (see Table 2). E3SMv1 performs better than
393 CESM1 and CESM2 because of its higher mass fraction of fine dust. Although DOD in MERRA-2 agrees
394 well with CALIOP DOD over the Atlantic, it tends to have much faster drop than CALIOP along the transport
395 pathway, especially between 20°W and 0° . This suggests that dust in MERRA-2 may also deposit too fast.
396 The decline rate of DOD in E3SMv1 agrees well with that in CALIOP. Because of the reduced geometric
397 standard deviation in the coarse mode in CESM2 (Table 1), dust dry deposition decreases, and dust lifetime
398 increases significantly, which explains the weak longitudinal gradient of DOD in CESM2. Similar
399 conclusions can be drawn from Fig. 6b for dust transport across the Pacific. CESM1, CESM2, and E3SMv1
400 underestimate DOD over the Pacific but overestimate DOD in source regions (i.e., Taklamakan and Gobi



401 Desert) of East Asia compared with CALIOP. DOD from MERRA-2 is higher than CALIOP over both East
402 Asia and the Pacific. Large disparities of DOD from CALIOP, MODIS, and MISR are found over both land
403 and ocean. CALIOP DOD is lower than MODIS DOD, and the differences are larger over land (~ 0.1). MISR
404 DOD over ocean is close to CALIOP DOD over the Atlantic and MODIS DOD over the Pacific.

405 Figure 7 shows the seasonal variations of modeled DOD in comparison with satellite retrievals from
406 CALIOP, MODIS, and MISR at 12 selected regions. In North Africa (Fig. 7a), CESM2 significantly
407 underestimates DOD in MAM, JJA, and SON due to its low dust emission (see Figs. 3a and 4a). DOD in
408 E3SMv1 agrees well with CALIOP DOD, while CESM1 and MERRA-2 overestimates DOD in all seasons
409 compared with CALIOP. Over the Atlantic (Fig. 7e), DOD in MERRA-2 agrees well with CALIOP DOD in
410 all seasons, while E3SMv1 underestimates DOD in MAM and JJA. This suggests that wet removal of dust
411 in E3SMv1 over the Atlantic in MAM and JJA may be too strong. In North America (Fig. 7i), CESM1,
412 CESM2, and E3SMv1 produces much lower DOD due to the underestimation of dust transport across the
413 Pacific. MODIS DOD peaks in July similar to the seasonality of trans-Atlantic dust transport, while CALIOP
414 DOD peaks in May similar to the seasonality of trans-Pacific dust transport. Unlike North Africa, all models
415 overestimate DOD in MAM, JJA, and SON compared with CALIOP in Northwest China (Fig. 7b) due to
416 overestimation of dust emission. Because E3SMv1 has larger dust emission than CESM1 and CESM2 in DJF
417 (Fig. 3b), the low bias of DOD is improved. This suggests that CESM1 and CESM2 may underestimate dust
418 emission in DJF over Northwest China. Over the Pacific (Fig 7f and j), DOD in E3SMv1 agrees well with
419 CALIOP DOD from May to October, while CESM1 and CESM2 underestimate DOD in all seasons,
420 especially in DJF by over one order of magnitude. DOD in all models and MODIS reaches its minimum in
421 December or January, whereas CALIOP DOD has its minimum in August.

422 Figure 7c, g, and k focus on the source regions in SH. The seasonal variations of DOD in SH are opposite



423 to NH due to opposite seasons in SH. CESM2 significantly overestimates DOD in all seasons compared with
424 CALIOP, by one order of magnitude due to the overestimation of dust emission, while CESM1, E3SMv1,
425 and MERRA-2 perform reasonably well. Figure 7d, h, and l focus on the three remote regions where the
426 largest disagreements between model simulations and observations are found. In the Arctic (Fig. 7d), CESM1,
427 CESM2, and E3SMv1 all have low biases of DOD, but E3SMv1 performs better than CESM1 and CESM2,
428 especially in DJF. CESM2 performs slightly better than CESM1 due to the reduced geometric standard
429 deviations in the accumulation and coarse mode. MERRA-2 overestimates DOD compared with CALIOP
430 due to excessive dust transport from NH source regions. Over the tropical Pacific (Fig. 7h), CALIOP, MODIS,
431 and MISR DOD all shows small seasonal contrast, while MERRA-2 shows considerable seasonal contrast of
432 DOD with its maximum in May and its minimum in November, which is influenced by dust transport over
433 the North Pacific. In the Southern Ocean (Fig. 7l), MODIS and MISR DOD has much stronger seasonal
434 variations than CALIOP DOD. Because of the assimilation of AOD, MERRA-2 also has opposite seasonal
435 variations to CALIOP DOD as MODIS and MISR. The difference in the seasonality of retrieved DOD may
436 come from cloud contamination over the Southern Ocean. In the selected regions, DOD from Y15 is generally
437 larger than that from L15, because the differences in retrieval algorithms lead to higher dust extinction in the
438 lower troposphere for Y15.

439

440 **3.3 Dust Extinction**

441 Figure 8 compares annual mean vertical profiles of modeled dust extinction with satellite retrievals from
442 L15 and Y15 in 12 selected regions. In North Africa (Fig. 8a), modeled dust extinction agrees well with
443 observations from L15 and Y15 in the lower and middle troposphere (> 500 hPa). In the upper troposphere
444 (< 400 hPa), significant high model biases of dust extinction are found in all models and over one order of



445 magnitude in CESM1 and MERRA-2, which comes from JJA and SON (see Figs. S2-S5). It is likely due to
446 excessive convective transport (e.g., Allen & Landuyt, 2014) and lack of secondary activation of aerosols
447 entrained into convective updrafts (e.g., Wang et al., 2013; Yu et al., 2019) in the models. As E3SMv1 uses a
448 unified aerosol convective transport scheme with secondary activation (Wang et al., 2013, 2020), the high
449 model biases of dust extinction are reduced. Due to its lower dust emission in North Africa (Fig. 3a), less
450 dust is lifted up throughout the troposphere in CESM2 than in the other models. MERRA-2 has the largest
451 high biases of dust extinction in the upper troposphere because of its highest fine mode mass fraction. As
452 dust is transported to the Atlantic, the dust extinction decreases at all levels (Fig. 8e). Dust extinction in
453 E3SMv1 agrees well with CALIOP. CESM1 underestimates dust extinction below 500 hPa but overestimates
454 dust extinction above 500 hPa. MERRA-2 agrees well with the observations below 500 hPa but is much
455 larger than observations in the upper troposphere. In North America (Fig. 8i), CESM1, CESM2, and E3SMv1
456 greatly underestimate dust extinction in the lower troposphere by one order of magnitude. The low model
457 biases reach the maximum in JJA (Fig. S3) and the minimum in DJF (Fig. S5). Since MERRA-2 has similar
458 dust emission as CESM1 and E3SMv1 but only slightly underestimates dust extinction in the lower
459 troposphere. The low biases of dust extinction in CESM1, CESM2, and E3SMv1 are mainly caused by the
460 underestimation of dust transport across the Pacific. We can see that in the Northeast Pacific (Fig. 8j),
461 MERRA-2 and L15 still has dust extinction of 0.001-0.002 km⁻¹ in the bottom layer. The high biases of dust
462 extinction in MERRA-2 above 600 hPa are consistent with the overly strong transport across the Atlantic and
463 Pacific.

464 As shown in Fig. 8b, f, and j, CESM1, CESM2, and E3SMv1 have high biases of dust extinction in
465 Northwest China but low biases over the Pacific. The magnitude of the low biases of dust extinction peaks
466 in DJF (Fig. S5), which corresponds to the low biases of DOD in Fig. 7. CALIOP dust extinction profiles



467 vary little across the Pacific, while dust extinction at all levels in CESM1, CESM2, and E3SMv1 decreases
468 notably, resulting in the increase of low biases of DOD with distance from the source. MERRA-2
469 overestimates dust extinction above 800 hPa over the Pacific and shows a slightly increase from 1000 hPa to
470 600 hPa. This indicates that MERRA-2 significantly overestimates the dust transport across the Pacific.
471 CESM2 significantly overestimates dust extinction at all levels in the three SH source regions (Fig. 8c, g,
472 and k) due to the overestimation of dust emission. In South America, CESM1 and E3SMv1 underestimate
473 dust extinction below 900 hPa. This suggests that the two models may underestimate the dust emission. In
474 the Arctic (Fig. 8d), E3SMv1 improves dust extinction at all levels compared with CESM1, while CESM2
475 only increases dust extinction below 800 hPa. Over the Southern Ocean, CESM1, CESM2, and E3SMv1 all
476 underestimate dust extinction below 850 hPa and produce an increase compared to the bottom level. The
477 overestimation of dust extinction above 800 hPa by MERRA-2 is also evident in Fig. 8d, h, and l. We note
478 that there are considerable differences between satellite retrievals from L15 and Y15. Dust extinction from
479 L15 is larger in the upper troposphere and lower in the lower troposphere than that from Y15, which is due
480 to different dust identification and separation methods (Wu et al., 2019).

481

482 **3.4 Dust Surface Concentration**

483 Figure 9 compares simulated annual mean dust surface concentrations with observations at 24 sites, as
484 shown in Fig. 1b. We use the dust surface concentrations for 0.2-12 μm (bins 1-4) in MERRA-2 for better
485 comparison with CESM1, CESM2, and E3SMv1. Note that all measurements of dust surface concentrations
486 except for observations at Barbados and Miami were conducted prior to 2007-2009. Some observations are
487 derived from measurements of aluminum by assuming a certain fraction. CESM1, CESM2, and E3SMv1
488 have low biases, while MERRA-2 has high biases at most sites. E3SMv1 performs better than CESM1 and



489 CESM2 in terms of the overall correlation (R), mean bias (MB), and mean normalized bias (MNB). CESM2
490 has the lowest correlation and the highest overall MB and MNB. The overall underestimation of dust surface
491 concentrations in CESM1, CESM2, and E3SMv1 mainly results from the low biases at sites in the Arctic,
492 Antarctic, and Tropical Pacific.

493 Figure 10 shows the seasonal variations of modeled dust surface concentrations in comparison with
494 observations at 12 selected sites. At Izana (Fig. 10a) which is close to the west coast of North Africa, all
495 models underestimate dust surface concentrations due to low dust emissions in Northwest Africa (15°W-5°E)
496 and fail to capture the seasonality. Although DOD in MERRA-2 agrees well with CALIOP observations over
497 the Atlantic (see Fig. 6a), MERRA-2 still has considerable low biases in dust surface concentrations because
498 of too much dust emitted in the fine mode. Dust surface concentrations in the four models agree better with
499 observations at Barbados (Fig. 10e) than at Miami (Fig. 10i). CESM1, CESM2, and E3SMv1 underestimate
500 dust surface concentrations at Miami, especially in DJF by more than one order of magnitude. E3SMv1 tends
501 to have the best agreement with observations at Cheju (Fig. 10b), while CESM1 and CESM2 have strong
502 low biases in JJA and DJF. MERRA-2 overestimates the concentrations at Midway Island and Oahu Hawaii
503 in all months.

504 Figure 10c, g, and k show three sites in NH high-latitude regions. E3SMv1 significantly improves the
505 dust surface concentrations compared with CESM1 and CESM2 at Alert, but it still has low biases, especially
506 in SON and DJF by one order of magnitude. Ground measurements show high dust surface concentrations
507 in SON due to local dust emission in NH high-latitude regions (Fan et al., 2013; Groot Zwaaftink et al., 2016),
508 but CESM1, CESM2, and E3SMv1 miss the local dust sources there. CESM1 and E3SMv1 tend to have
509 stronger low model biases of dust surface concentrations at Heimaey than at Alert, while CESM2 tend to
510 have weaker low model biases at Heimaey than at Alert, especially in DJF. Figure 10d, h, and l show three



511 sites in the Tropical Pacific and Antarctic. At Palmer Station, CESM1 underestimates dust surface
512 concentrations by three orders of magnitude. Dust surface concentrations in CESM2 are higher than CESM1
513 and E3SMv1 due to higher dust emission in SH and the reduced geometric standard deviations. Because
514 E3SMv1 produces small amount of dust emission in the Antarctic (Fig. 2c), it also has higher concentrations.

515

516 **4 Discussion and Conclusions**

517 In this study, we evaluate the spatiotemporal variations of dust extinction profiles and DOD in CESM1,
518 CESM2, E3SMv1, and MERRA-2 against satellite retrievals from CALIOP (L15 and Y15), MODIS, and
519 MISR. We find that CESM1, CESM2, and E3SMv1 underestimate global annual mean DOD compared with
520 CALIOP and MODIS, which can be mainly attributed to the low model biases of DOD over ocean. This
521 indicates that CESM1, CESM2, and E3SMv1 underestimate dust transport to remote regions. E3SMv1
522 performs better than CESM1 and CESM2 in NH due to its higher fine mode mass fraction of dust. CESM2
523 performs the worst in NH due to its lower dust emission but improves DOD in SH due to its high dust
524 emissions in SH source regions. DOD in MERRA-2 agrees well with CALIOP DOD in remote regions due
525 to the assimilation of AOD and its higher mass fraction of fine mode dust. All models tend to overestimate
526 dust extinction in the upper troposphere of source regions because of excessive convective transport and/or
527 lack of secondary activation of aerosols entrained into convective updrafts. The latter is considered in
528 E3SMv1 (Wang et al., 2020), which thus shows a reduced bias of dust extinction in the upper troposphere.
529 The high model biases of dust extinction in MERRA-2 in the upper troposphere are persistent around the
530 globe.

531 CESM1, CESM2, and E3SMv1 produce substantial greater DOD than CALIOP in Northeast Africa and
532 fail to capture the spatial distributions of DOD in North Africa, which can be significantly improved by using



533 the source function of Ginoux et al. (2001) or the dust emission scheme of Kok et al. (2014a, 2014b) (K14).
534 The three models also overestimate DOD over Northwest China due to the overestimation of dust emission
535 in MAM, JJA, and SON. Wu et al. (2019) showed that CESM1 with K14 dust emission scheme better agrees
536 with CALIOP observations in Northwest China. Since the source functions used in the four models are all
537 zeros north to 60°N, the four models don't produce any dust emissions in NH high-latitude regions, while
538 ground observations indicate considerable local dust sources.

539 The low model biases of DOD over the Atlantic in CESM1, CESM2, and E3SMv1 can be greatly
540 improved if the high dust emission in Northeast Africa is captured by models. E3SMv1 has similar decline
541 rate of DOD as CALIOP from Northeast Africa to the Atlantic. CESM1, CESM2, and E3SMv1 underestimate
542 DOD in remote regions resulting from too fast dust deposition. Wu et al. (2018) showed that lower dry
543 deposition velocities for fine particles results in higher dust concentrations in remote regions (see Figure S1).
544 Dust emission in the three models is only added to the bottom layer currently, while dust storms in reality
545 can bring dust to high altitudes. The turbulent mixing of dust in the boundary layer needs to be improved.

546 Substantial differences are also found between MODIS and CALIOP DOD, which can greatly affect
547 model evaluation. MODIS DOD (> 0.06) is significantly larger than CALIOP DOD (< 0.03). DOD over
548 ocean from MISR is between MODIS and CALIOP. The differences between MODIS and CALIOP DOD
549 may come from instrument differences, artifacts such as cloud contamination and calibration issues, and
550 different retrieval algorithms. Ground lidar measurements, such as the Micro-Pulse Lidar Network
551 (MPLNET) and the European Aerosol Research Lidar Network (EARLINET), are needed to validate the
552 satellite retrievals from CALIOP, MODIS, and MISR.

553

554 **Code Availability**



555 The CESM1.2 source code is available at <https://github.com/YamataSensei/CESM-code>. The CESM2.1
556 source code is available at <https://github.com/ESCOMP/cesm>. The E3SMv1 source code is available at
557 <https://github.com/E3SM-Project/E3SM>.

558

559 **Data Availability**

560 The model output of CESM1 and CESM2 is archived at NCAR Cheyenne supercomputer. The model output
561 of E3SMv1 is archived at NERSC Cori supercomputer. MERRA-2 data is available at
562 <https://disc.gsfc.nasa.gov/>. CALIOP, MODIS and MISR data can be obtained online at
563 <https://search.earthdata.nasa.gov>.

564

565 **Author Contribution**

566 MW and XL conceived the project. MW designed and ran the model simulations with help and input from
567 XL, YS, CW, and ZK. HY, KY, TL, and ZW derived dust extinction profiles from CALIOP. AD derived dust
568 extinction profiles from MERRA-2. MW led the analysis and wrote the first draft of the paper. All coauthors
569 participated in discussions on data analysis and revised the paper.

570

571 **Competing Interests**

572 The authors declare that they have no conflict of interest.

573

574 **Acknowledgement**

575 This work is supported by NASA CloudSat and CALIPSO Science Program (grant NNX16AO94G). This
576 work is also funded by the U.S. Department of Energy (DOE), Office of Science, Office of Biological and



577 Environmental Research, Earth and Environmental System Modeling program as part of the Energy Exascale
578 Earth System Model (E3SM) project. The Pacific Northwest National Laboratory (PNNL) is operated for
579 DOE by Battelle Memorial Institute under contract DE-AC05-76RLO1830. We would like to acknowledge
580 the use of computational resources for conducting the model simulations at the National Energy Research
581 Scientific Computing Center (NERSC), a U.S. DOE Office of Science User Facility operated under contract
582 DE-AC02-05CH11231, and the NCAR-Wyoming Supercomputing Center provided by the NSF and the State
583 of Wyoming and supported by NCAR's Computational and Information Systems Laboratory. We would like
584 to thank Dr. Paul Ginoux for providing MODIS DOD over land, Dr. Joseph M. Prospero for providing the
585 measurements of dust surface concentrations at Heimaey, Barbados, and Miami, and Dr. Songmiao Fan for
586 providing the measurements of dust surface concentrations at Alert.

587

588 **References**

589 Allen, R. J., and Landuyt, W.: The vertical distribution of black carbon in CMIP5 models: Comparison to
590 observations and the importance of convective transport, *J. Geophys. Res.-Atmos.*, 119, 4808-4835,
591 <https://doi.org/10.1002/2014JD021595>, 2014.

592 Amiridis, V., Wandinger, U., Marinou, E., Giannakaki, E., Tsekeri, A., Basart, S., Kazadzis, S., Gkikas, A.,
593 Taylor, M., Baldasano, J., and Ansmann, A.: Optimizing CALIPSO Saharan dust retrievals, *Atmos. Chem.*
594 *Phys.*, 13, 12089-12106, <https://doi.org/10.5194/acp-13-12089-2013>, 2013.

595 Anderson, T. L., Wu, Y., Chu, D. A., Schmid, B., Redemann, J., and Dubovik, O.: Testing the MODIS satellite
596 retrieval of aerosol fine-mode fraction, *J. Geophys. Res.*, 110, D18204,
597 <https://doi.org/10.1029/2005JD005978>, 2005.

598 Arimoto, R., Duce, R. A., Savoie, D. L., Prospero, J. M., Talbot, R., Cullen, J. D., Tomza, U., Lewis, N. F.,



599 and Ray, B. J.: Relationships among aerosol constituents from Asia and the North Pacific during PEM-
600 West A, *J. Geophys. Res.*, 101, 2011-2023, <https://doi.org/10.1029/95JD01071>, 1996.

601 Balkanski, Y., Schulz, M., Claquin, T., and Guibert, S.: Reevaluation of Mineral aerosol radiative forcings
602 suggests a better agreement with satellite and AERONET data, *Atmos. Chem. Phys.*, 7, 81-95,
603 <https://doi.org/10.5194/acp-7-81-2007>, 2007.

604 Baddock, M. C., Ginoux, P., Bullard, J. E., and Gill, T. E.: Do MODIS-defined dust sources have a
605 geomorphological signature?, *Geophys. Res. Lett.*, 43, 2606-2613,
606 <https://doi.org/10.1002/2015GL067327>, 2016.

607 Bogenschutz, P. A., Gettelman, A., Morrison, H., Larson, V. E., Craig, C., and Schanen, D. P.: Higher-order
608 turbulence closure and its impact on climate simulations in the Community Atmosphere Model, *J. Climate*,
609 26, 9655-9676, <https://doi.org/10.1175/JCLI-D-13-00075.1>, 2013.

610 Boucher, O., Randall, D., Artaxo, P., Bretherton, C., Feingold, G., Forster, P., Kerminen, V.-M., Kondo, Y.,
611 Liao, H., Lohmann, U., Rasch, P., Satheesh, S. K., Sherwood, S., Stevens, B., and Zhang, X. Y.: Clouds
612 and aerosols, in: *Climate change 2013: the physical science basis. Contribution of Working Group I to the*
613 *Fifth Assessment Report of the Intergovernmental Panel on Climate Change*, Cambridge University Press,
614 Cambridge, United Kingdom and New York, NY, USA, 2013

615 Chin, M., Ginoux, P., Kinne, S., Torres, O., Holben, B. N., Duncan, B. N., Martin, R. V., Logan, J. A.,
616 Higurashi, A., and Nakajima, T.: Tropospheric aerosol optical thickness from the GOCART model and
617 comparisons with satellite and sun photometer measurements, *J. Atmos. Sci.*, 59, 461-483,
618 [https://doi.org/10.1175/1520-0469\(2002\)059<0461:TAOTFT>2.0.CO;2](https://doi.org/10.1175/1520-0469(2002)059<0461:TAOTFT>2.0.CO;2), 2002.

619 DeMott, P. J., Sassen, K., Poellot, M. R., Baumgardner, D., Rogers, D. C., Brooks, S. D., Prenni, A. J., and
620 Kreidenweis, S. M.: African dust aerosols as atmospheric ice nuclei, *Geophys. Res. Lett.*, 30(14), 1732,



- 621 <https://doi.org/10.1029/2003GL017410>, 2013.
- 622 Dentener, F. J., Carmichael, G. R., Zhang, Y., Lelieveld, J., and Crutzen, P. J.: Role of mineral aerosol as a
623 reactive surface in the global troposphere, *J. Geophys. Res.*, 101, 22869-22889,
624 <https://doi.org/10.1029/96JD01818>, 1996.
- 625 Evan, A. T., Flamant, C., Fiedler, S. and Doherty, O.: An analysis of aeolian dust in climate models, *Geophys.*
626 *Res. Lett.*, 41, 5996-6001, <https://doi.org/10.1002/2014GL060545>, 2014.
- 627 Fan, S.-M.: Modeling of observed mineral dust aerosols in the arctic and the impact on winter season low
628 level clouds, *J. Geophys. Res.-Atmos.*, 118, 11161-11174, <https://doi.org/10.1002/jgrd.50842>, 2013.
- 629 Gelaro, R., McCarty, W., Suárez, M. J., Todling, R., Molod, A., Takacs, L., Randles, C. A., Darmenov, A.,
630 Bosilovich, M. G., Reichle, R., Wargan, K., Coy, L., Cullather, R., Draper, C., Akella, S., Buchard, V.,
631 Conaty, A., da Silva, A. M., Gu, W., Kim, G.-K., Koster, R., Lucchesi, R., Merkova, D., Nielsen, J. E.,
632 Partyka, G., Pawson, S., Putman, W., Rienecker, M., Schubert, S. D., Sienkiewicz, M., and Zhao, B.: The
633 Modern-Era Retrospective Analysis for Research and Applications, Version 2 (MERRA-2), *J. Climate*, 30,
634 5419-5454, <https://doi.org/10.1175/JCLI-D-16-0758.1>, 2017.
- 635 Gettelman, A., and Morrison, H.: Advanced two-moment bulk microphysics for global models. Part I: Off-
636 line tests and comparison with other schemes, *J. Climate*, 28, 1268-1287, <https://doi.org/10.1175/JCLI-D-14-00102.1>, 2015.
- 638 Ginoux, P., Chin, M., Tegen, I., Prospero, J. M., Holben, B., Dubovik, O., and Lin, S.-J.: Sources and
639 distributions of dust aerosols simulated with the GOCART model, *J. Geophys. Res.*, 106, 20255-20273,
640 <https://doi.org/10.1029/2000JD000053>, 2001.
- 641 Golaz, J.C., Larson, V. E., and Cotton, W. R.: A pdf-based model for boundary layer clouds. Part I: Method
642 and model description, *J. Atmos. Sci.*, 59, 3540-3551, <https://doi.org/10.1175/1520->



- 643 0469(2002)059<3540:APBMFB>2.0.CO;2, 2002.
- 644 Golaz, J.-C., Caldwell, P. M., Van Roekel, L. P., Petersen, M. R., Tang, Q., Wolfe, J. D., Abeshu, G.,
645 Anantharaj, V., Asay-Davis, X. S., Bader, D. C., Baldwin, S. A., Bisht, G., Bogenschütz, P. A., Branstetter,
646 M., Brunke, M. A., Brus, S. R., Burrows, S. M., Cameron-Smith, P. J., Donahue, A. S., Deakin, M., Easter,
647 R. C., Evans, K. J., Feng, Y., Flanner, M., Foucar, J. G., Fyke, J. G., Griffin, B. M., Hannay, C., Harrop, B.
648 E., Hoffman, M. J., Hunke, E. C., Jacob, R. L., Jacobsen, D. W., Jeffery, N., Jones, P. W., Keen, N. D.,
649 Klein, S. A., Larson, V. E., Leung, L. R., Li, H.-Y., Lin, W., Lipscomb, W. H., Ma, P.-L., Mahajan, S.,
650 Maltrud, M. E., Mamejtanov, A., McClean, J. L., McCoy, R. B., Neale, R. B., Price, S. F., Qian, Y., Rasch,
651 P. J., Reeves Eyre, J. E. J., Riley, W. J., Ringler, T. D., Roberts, A. F., Roesler, E. L., Salinger, A. G.,
652 Shaheen, Z., Shi, X., Singh, B., Tang, J., Taylor, M. A., Thornton, P. E., Turner, A. K., Veneziani, M., Wan,
653 H., Wang, H., Wang, S., Williams, D. N., Wolfram, P. J., Worley, P. H., Xie, S., Yang, Y., Yoon, J.-H.,
654 Zelinka, M. D., Zender, C. S., Zeng, X., Zhang, C., Zhang, K., Zhang, Y., Zheng, X., Zhou, T., Zhu, Q.:
655 The DOE E3SM coupled model version 1: Overview and evaluation at standard resolution, *J. Adv. Model.*
656 *Earth Sy.*, 11, <https://doi.org/10.1029/2018MS001603>, 2019.
- 657 Groot Zwaafink, C. D., Grythe, H., Skov, H., and Stohl, A.: Substantial contribution of northern high-latitude
658 sources to mineral dust in the Arctic, *J. Geophys. Res.-Atmos.*, 121, 13678-13697,
659 <https://doi.org/10.1002/2016JD025482>, 2016.
- 660 Hsu, N. C., Jeong, M.-J., Bettenhausen, C., Sayer, A. M., Hansell, R., Seftor, C. S., Huang, J., and Tsay, S.-
661 C.: Enhanced Deep Blue aerosol retrieval algorithm: The second generation, *J. Geophys. Res.-Atmos.*, 118,
662 9296-9315, <https://doi.org/10.1002/jgrd.50712>, 2013.
- 663 Huneus, N., Schulz, M., Balkanski, Y., Griesfeller, J., Prospero, J., Kinne, S., Bauer, S., Boucher, O., Chin,
664 M., Dentener, F., Diehl, T., Easter, R., Fillmore, D., Ghan, S., Ginoux, P., Grini, A., Horowitz, L., Koch,



665 D., Krol, M. C., Landing, W., Liu, X., Mahowald, N., Miller, R., Morcrette, J.-J., Myhre, G., Penner, J.,
666 Perlwitz, J., Stier, P., Takemura, T., and Zender, C. S.: Global dust model intercomparison in AeroCom
667 phase I, *Atmos. Chem. Phys.*, 11, 7781-7816, <https://doi.org/10.5194/acp-11-7781-2011>, 2011.

668 Hurrell, J. W., Holland, M. M., Gent, P. R., Ghan, S., Kay, J. E., Kushner, P. J., Lamarque, J.-F., Large, W.
669 G., Lawrence, D., Lindsay, K., Lipscomb, W. H., Long, M. C., Mahowald, N., Marsh, D. R., Neale, R. B.,
670 Rasch, P., Vavrus, S., Vertenstein, M., Bader, D., Collins, W. D., Hack, J. J., Kiehl, J., Marshall, S.: The
671 Community Earth System Model: A framework for collaborative research, *Bull. Amer. Meteor. Soc.*, 94(9),
672 1339-1360, <https://doi.org/10.1175/BAMS-D-12-00121.1>, 2013.

673 Jickells, T. D., An, Z. S., Anderson, K. K., Baker, A. R., Bergametti, G., Brooks, N., Cao, J. J., Boyd, P. W.,
674 Duce, R. A., Hunter, K. A., Kawahata, H., Kubilay, N., IaRoche, J., Liss, P. S., Mahowald, N., Prospero, J.
675 M., Ridgwell, A. J., Tegen, I., and Torres, R.: Global iron connections between desert dust, ocean
676 biogeochemistry, and climate, *Science*, 308, 67-71, <https://doi.org/10.1126/science.1105959>, 2005.

677 Johnson, M. S., Meskhidze, N., and Praju Kiliyanpilakkil, V.: A global comparison of GEOS-Chem-predicted
678 and remotely-sensed mineral dust aerosol optical depth and extinction profiles, *J. Adv. Model. Earth Sy.*,
679 4, M07001, <https://doi.org/10.1029/2011MS000109>, 2012.

680 Kaufman, Y. J., Koren, I., Remer, L. A., Tanré, D., Ginoux, P., and Fan, S.: Dust transport and deposition
681 observed from the Terra-Moderate Resolution Imaging Spectroradiometer (MODIS) spacecraft over the
682 Atlantic Ocean, *J. Geophys. Res.*, 110, D10S12, <https://doi.org/2003JD004436>, 2005.

683 Kim, D., Chin, M., Yu, H., Diehl, T., Tan, Q., Kahn, R. A., Tsigaridis, K., Bauer, S. E., Takemura, T., Pozzoli,
684 L., Bellouin, N., Schulz, M., Peyridieu, S., Chédin, A., and Koffi, B.: Sources, sinks, and transatlantic
685 transport of North African dust aerosol: A multimodel analysis and comparison with remote sensing data,
686 *J. Geophys. Res.-Atmos.*, 119, 6259-6277, <https://doi.org/10.1002/2013JD021099>, 2014.



- 687 Kim, D., Chin, M., Yu, H., Pan, X., Bian, H., and Tan, Q.: Asian and trans-pacific dust: A multimodel and
688 multiremote sensing observation analysis, *J. Geophys. Res.-Atmos.*, 124,
689 <https://doi.org/10.1029/2019JD030822>, 2019.
- 690 Kok, J. F.: A scaling theory for the size distribution of emitted dust aerosols suggests climate models
691 underestimate the size of the global dust cycle, *P. Natl. Acad. Sci. USA.*, 108, 1016-1021,
692 <https://doi.org/10.1073/pnas.1014798108>, 2011.
- 693 Kok, J. F., Mahowald, N. M., Fratini, G., Gillies, J. A., Ishizuka, M., Leys, J. F., Mikami, M., Park, M.-S.,
694 Park, S.-U., Van Pelt, R. S., and Zobeck, T. M.: An improved dust emission model – Part 1: Model
695 description and comparison against measurements, *Atmos. Chem. Phys.*, 14, 13023–13041,
696 <https://doi.org/10.5194/acp-14-13023-2014>, 2014a.
- 697 Kok, J. F., Albani, S., Mahowald, N. M., and Ward, D. S.: An improved dust emission model – Part 2:
698 Evaluation in the Community Earth System Model, with implications for the use of dust source functions,
699 *Atmos. Chem. Phys.*, 14, 13043–13061, <https://doi.org/10.5194/acp-14-13043-2014>, 2014b.
- 700 Kok, J. F., Ridley, D. A., Zhou, Q., Miller, R. L., Zhao, C., Heald, C. L., Ward, D. S., Albani, S., and Haustein,
701 K.: Smaller desert dust cooling effect estimated from analysis of dust size and abundance, *Nat. Geosci.*,
702 10, 274-278, <https://doi.org/10.1038/NGEO2912>, 2017.
- 703 Lawrence, D., Fisher, R., Koven, C., Oleson, K., Swenson, S., Vertenstein, M., Andre, B., Bonan, G., Ghimire,
704 B., van Kampenhout, L., Kennedy, D., Kluzek, E., Knox, R., Lawrence, P., Li, F., Li, H., Lombardozzi, D.,
705 Lu, Y., Perket, J., Riley, W., Sacks, W., Shi, M., Wieder, W., Xu, C., Ali, A., Badger, A., Bisht, G., Broxton,
706 P., Brunke, M., Buzan, J., Clark, M., Craig, T., Dahlin, K., Drewniak, B., Emmons, L., Fisher, J., Flanner,
707 M., Gentine, P., Lenaerts, J., Levis, S., Leung, L. R., Lipscomb, W., Pelletier, J., Ricciuto, D. M., Sanderson,
708 B., Shuman, J., Slater, A., Subin, Z., Tang, J., Tawfik, A., Thomas, Q., Tilmes, S., Vitt, F., Zeng, X.:



- 709 Technical description of version 5.0 of the Community Land Model (CLM),
710 http://www.cesm.ucar.edu/models/cesm2/land/CLM50_Tech_Note.pdf, 2019.
- 711 Levy, R. C., Mattoo, S., Sawyer, V., Shi, Y., Colarco, P. R., Lyapustin, A. I., Wang, Y., and Remer, L. A.:
712 Exploring systematic offsets between aerosol products from the two MODIS sensors, *Atmos. Meas. Tech.*,
713 11, 4073-4092, <https://doi.org/10.5194/amt-11-4073-2018>, 2018.
- 714 Liu, X., Ma, P.-L., Wang, H., Tilmes, S., Singh, B., Easter, R. C., Ghan, S. J., and Rasch, P. J.: Description
715 and evaluation of a new four-mode version of the Modal Aerosol Module (MAM4) within version 5.3 of
716 the Community Atmosphere Model, *Geosci. Model Dev.*, 9, 505-522, [https://doi.org/10.5194/gmd-9-505-](https://doi.org/10.5194/gmd-9-505-2016)
717 2016, 2016.
- 718 Luo, T., Wang, Z., Ferrare, R. A., Hostetler, C. A., Yuan, R., and Zhang, D.: Vertically resolved separation of
719 dust and other aerosol types by a new lidar depolarization method, *Opt. Express*, 23(11), 14095-14107,
720 <https://doi.org/10.1364/OE.23.014095>, 2015a.
- 721 Luo, T., Wang, Z., Zhang, D., Liu, X., Wang, Y., and Yuan, R.: Global dust distribution from improved thin
722 dust layer detection using A-train satellite lidar observations, *Geophys. Res. Lett.*, 42, 620-628,
723 <https://doi.org/10.1002/2014GL062111>, 2015b.
- 724 Ma, X., Bartlett, K., Harmon, K., and Yu, F.: Comparison of AOD between CALIPSO and MODIS:
725 significant differences over major dust and biomass burning regions, *Atmos. Meas. Tech.*, 6, 2391-2401,
726 <https://doi.org/10.5194/amt-6-2391-2013>, 2013.
- 727 Ma, X., and Yu, F.: Seasonal and spatial variations of global aerosol optical depth: multi-year modelling with
728 GEOS-Chem-APM and comparisons with multiple-platform observations, *Tellus B*, 67, 25115,
729 <https://doi.org/10.3402/tellusb.v67.25115>, 2015.
- 730 Neale, R. B., Chen, C.-C., Gettelman, A., Lauritzen, P. H., Park, S., Williamson, D. L., Conley, A. J., Garcia,



731 R., Kinnison, D., Lamarque, J.-F., Marsh, D., Mills, M., Smith, A. K., Tilmes, S., Vitt, F., Morrison, H.,
732 Cameron-Smith, P., Collins, W. D., Iacono, M. J., Easter, R. C., Ghan, S. J., Liu, X., Rasch, P. J., and Taylor,
733 M. A.: Description of the NCAR Community Atmosphere Model (CAM 5.0), NCAR Technical Note
734 NCAR/TN-486+ STR, http://www.cesm.ucar.edu/models/cesm1.2/cam/docs/description/cam5_desc.pdf,
735 2010.

736 Oleson, K. W., Lawrence, D. W., Bonan, G. B., Flanner, M. G., Kluzek, E., Lawrence, P. J., Levis, S.,
737 Swenson, S. C., Thornton, P. E., Dai, A., Decker, M., Dickinson, R., Feddema, J., Heald, C. L., Hoffman,
738 F., Lamarque, J.-F., Mahowald, N., Niu, G.-Y., Qian, T., Randerson, J., Running, S., Sakaguchi, K., Slater,
739 A., Stöckli, R., Wang, A., Yang, Z.-L., Zeng, X., Zeng, X.: Technical description of version 4.0 of the
740 Community Land Model (CLM), NCAR Technical Note NCAR/TN-478+STR,
741 http://www.cesm.ucar.edu/models/cesm1.2/clm/CLM4_Tech_Note.pdf, 2010.

742 Proestakis, E., Amiridis, V., Marinou, E., Georgoulas, A. K., Solomos, S., Kazadzis, S., Chimot, J., Che, H.,
743 Alexandri, G., Biniotoglou, I., Daskalopoulou, V., Kourtidis, K. A., de Leeuw, G., and van der A, R. J.:
744 Nine-year spatial and temporal evolution of desert dust aerosols over South and East Asia as revealed by
745 CALIOP, *Atmos. Chem. Phys.*, 18, 1337-1362, <https://doi.org/10.5194/acp-18-1337-2018>, 2018.

746 Prospero, J. M., Uematsu, M., and Savoie, D. L.: Mineral aerosol transport to the Pacific Ocean, in: *Chemical*
747 *oceanography*, Vol. 10, 188-218, New York, Academic Press, 1989.

748 Prospero, J. M.: The atmospheric transport of particles to the ocean, in: *Particle flux in the ocean*, Vol. 57,
749 19-52, New York, John Wiley & Sons Ltd, 1996.

750 Prospero, J. M., Bullard, J. E., and Hodgkins, R.: High-latitude dust over the North Atlantic: Inputs from
751 Icelandic proglacial dust storms, *Science*, 335, 1078-1082, <https://doi.org/10.1126/science.1217447>, 2012.

752 Pu, B. and Ginoux, P.: The impact of the Pacific Decadal Oscillation on springtime dust activity in Syria,



- 753 Atmos. Chem. Phys., 16, 13431-13448, <https://doi.org/10.5194/acp-16-13431-2016>, 2016.
- 754 Pu, B. and Ginoux, P.: How reliable are CMIP5 models in simulating dust optical depth?, Atmos. Chem.
755 Phys., 18, 12491-12510, <https://doi.org/10.5194/acp-18-12491-2018>, 2018.
- 756 Rahimi, S., Liu, X., Wu, C., Lau, W. K., Brown, H., Wu, M., and Qian, Y.: Quantifying snow-darkening and
757 atmospheric radiative effects of black carbon and dust on the South-Asian Monsoon and hydrological cycle:
758 Experiments using variable resolution CESM, Atmos. Chem. Phys., <https://doi.org/10.5194/acp-2019-195>,
759 2019.
- 760 Rasch, P. J., Xie, S., Ma, P.-L., Lin, W., Wang, H., Tang, Q., Burrows, S. M., Caldwell, P., Zhang, K., Easter,
761 R. C., Cameron-Smith, P., Singh, B., Wan, H., Golaz, J.-C., Harrop, B. E., Roesler, E., Bacmeister, J.,
762 Larson, V. E., Evans, K. J., Qian, Y., Taylor, M., Leung, L. R., Zhang, Y., Brent, L., Branstetter, M., Hannay,
763 C., Mahajan, S., Mametjanov, A., Neale, R., Richter, J. H., Yoon, J.-H., Zender, C. S., Bader, D., Flanner,
764 M., Foucar, J. G., Jacob, R., Keen, N., Klein, S. A., Liu, X., Salinger, A. G., Shrivastava, M., and Yang, Y.:
765 An overview of the atmospheric component of the Energy Exascale Earth System Model, J. Adv. Model.
766 Earth Sy., 11, 2377-2411, <https://doi.org/10.1029/2019MS001629>, 2019.
- 767 Ridley, D. A., Heald, C. L., Kok, J. F., and Zhao, C.: An observationally constrained estimate of global dust
768 aerosol optical depth, Atmos. Chem. Phys., 16, 15097-15117, <https://doi.org/10.5194/acp-16-15097-2016>,
769 2016.
- 770 Rosenfeld, D., Rudich, Y., and Lahav, R.: Desert dust suppressing precipitation: A possible desertification
771 feedback loop, P. Natl. Acad. Sci. USA, 98, 5975-5980, <https://doi.org/10.1073/pnas.101122798>, 2001.
- 772 Scanza, R. A., Mahowald, N., Ghan, S., Zender, C. S., Kok, J. F., Liu, X., Zhang, Y., and Albani, S.: Modeling
773 dust as component minerals in the Community Atmosphere Model: development of framework and impact
774 on radiative forcing, Atmos. Chem. Phys., 15, 537-561, <https://doi.org/10.5194/acp-15-537-2015>, 2015.



- 775 Shi, Y., and Liu, X.: Dust radiative effects on climate by glaciating mixed-phase clouds, *Geophys. Res. Lett.*,
776 46, <https://doi.org/10.1029/2019GL082504>, 2019.
- 777 Tegen, I., and Lacis, A. A.: Modeling of particle size distribution and its influence on the radiative properties
778 of mineral dust aerosol, *J. Geophys. Res.*, 101, 19237-19244, <https://doi.org/10.1029/95JD03610>, 1996.
- 779 Tegen, I., Lacis, A. A., and Fung, I.: The influence on climate forcing of mineral aerosols from disturbed
780 soils, *Nature*, 380, 419-422, <https://doi.org/10.1038/380419a0>, 1996.
- 781 Wandinger, U., Tesche, M., Seifert, P., Ansmann, A., Müller, D., and Althausen, D.: Size matters: Influence
782 of multiple scattering on CALIPSO light-extinction profiling in desert dust, *Geophys. Res. Lett.*, 37,
783 L10801, <https://doi.org/10.1029/2010GL042815>, 2010.
- 784 Wang, H., Easter, R. C., Rasch, P. J., Wang, M., Liu, X., Ghan, S. J., Qian, Y., Yoon, J.-H., Ma, P.-L., and
785 Vinoj, V.: Sensitivity of remote aerosol distributions to representation of cloud–aerosol interactions in a
786 global climate model, *Geosci. Model Dev.*, 6, 765-782, <https://doi.org/10.5194/gmd-6-765-2013>, 2013.
- 787 Wang, H., Easter, R. C., Zhang, R., Ma, P.-L., Singh, B., Zhang, K., Ganguly, D., Rasch, P. J., Burrows, S.
788 M., Ghan, S. J., Lou, S., Qian, Y., Yang, Y., Feng, Y., Flanner, M., Leung, R. L., Liu, X., Shrivastava, M.,
789 Sun, J., Tang, Q., Xie, S., and Yoon, J.-H.: Aerosols in the E3SM Version 1: New developments and their
790 impacts on radiative forcing, *J. Adv. Model. Earth Sy.*, 12, e2019MS001851,
791 <https://doi.org/10.1029/2019MS001851>, 2020.
- 792 Witek, M. L., Garay, M. J., Diner, D. J., Bull, M. A., and Seidel, F. C.: New approach to the retrieval of AOD
793 and its uncertainty from MISR observations over dark water, *Atmos. Meas. Tech.*, 11, 429-439,
794 <https://doi.org/10.5194/amt-11-429-2018>, 2018.
- 795 Wu, C., Lin, Z., Liu, X., Li, Y., Lu, Z., and Wu, M.: Can climate models reproduce the decadal change of
796 dust aerosol in East Asia?, *Geophys. Res. Lett.*, 45, 9953-9962, <https://doi.org/10.1029/2018GL079376>,



- 797 2018a.
- 798 Wu, C., Liu, X., Lin, Z., Rahimi-Esfarjani, S. R., and Lu, Z.: Impacts of absorbing aerosol deposition on
799 snowpack and hydrologic cycle in the Rocky Mountain region based on variable-resolution CESM (VR-
800 CESM) simulations, *Atmos. Chem. Phys.*, 18, 511-533, <https://doi.org/10.5194/acp-18-511-2018>, 2018b.
- 801 Wu, M., Liu, X., Zhang, L., Wu, C., Lu, Z., Ma, P.-L., Wang, H., Tilmes, S., Mahowald, N., Matsui, H., and
802 Easter, R. C.: Impacts of aerosol dry deposition on black carbon spatial distributions and radiative effects
803 in the Community Atmosphere Model CAM5, *J. Adv. Model. Earth Sy.*, 10, 1150-1171,
804 <https://doi.org/10.1029/2017MS001219>, 2018.
- 805 Wu, M., Liu, X., Yang, K., Luo, T., Wang, Z., Wu, C., Zhang, K., Yu, H., and Darmenov, A.: Modeling dust
806 in East Asia by CESM and sources of biases, *J. Geophys. Res.-Atmos.*, 124,
807 <https://doi.org/10.1029/2019JD030799>, 2019.
- 808 Yasunari, T. J., Koster, R. D., Lau, W. K. M., and Kim, K.-M.: Impact of snow darkening via dust, black
809 carbon, and organic carbon on boreal spring climate in the Earth system, *J. Geophys. Res.-Atmos.*, 120,
810 5485-5503, <https://doi.org/10.1002/2014JD022977>, 2015.
- 811 Yu, H., Chin, M., Remer, L. A., Kleidman, R. G., Bellouin, N., Bian, H., and Diehl, T.: Variability of marine
812 aerosol fine-mode fraction and estimates of anthropogenic aerosol component over cloud-free oceans from
813 the Moderate Resolution Imaging Spectroradiometer (MODIS), *J. Geophys. Res.*, 114, D10206,
814 <https://doi.org/10.1029/2008JD010648>, 2009.
- 815 Yu, H., Chin, M., Winker, D. M., Omar, A. H., Liu, Z., Kittaka, C., and Thomas, D.: Global view of aerosol
816 vertical distributions from CALIPSO lidar measurements and GOCART simulations: Regional and
817 seasonal variations, *J. Geophys. Res.*, 115, D00H30, <https://doi.org/10.1029/2009JD013364>, 2010.
- 818 Yu, H., Remer, L. A., Chin, M., Bian, H., Tan, Q., Yuan, T., and Zhang, Y.: Aerosols from overseas rival



819 domestic emissions over North America, *Science*, 337, 566-569, <https://doi.org/10.1126/science.1217576>,
820 2012.

821 Yu, H., Chin, M., Bian, H., Yuan, T., Prospero, J. M., Omar, A. H., Remer, L. A., Winker, D. M., Yang, Y.,
822 Zhang, Y., Zhang, Z.: Quantification of trans-Atlantic dust transport from seven-year (2007-2013) record
823 of CALIPSO lidar measurements, *Remote Sens. Environ.*, 159, 232-249,
824 <https://doi.org/10.1016/j.rse.2014.12.010>, 2015.

825 Yu, H., Tan, Q., Chin, M., Remer, L. A., Kahn, R. A., Bian, H., Kim, D., Zhang, Z., Yuan, T., Omar, A. H.,
826 Winker, D. M., Levy, R. C., Kalashnikova, O., Crepeau, L., Capelle, V., and Chédin, A.: Estimates of
827 African dust deposition along the trans-Atlantic transit using the decadelong record of aerosol
828 measurements from CALIOP, MODIS, MISR, and IASI, *J. Geophys. Res.-Atmos.*, 124, 7975-7996,
829 <https://doi.org/10.1029/2019JD030574>, 2019.

830 Yu, P., Froyd, K. D., Portmann, R. W., Toon, O. B., Freitas, S. R., Bardeen, C. G., Brock, C., Fan, T., Gao,
831 R.-S., Katich, J. M., Kupc, A., Liu, S., Maloney, C., Murphy, D. M., Rosenlof, K. H., Schill, G., Schwarz,
832 J. P., and Williamson, C.: Efficient in-cloud removal of aerosols by deep convection, *Geophys. Res. Lett.*,
833 46, 1061-1069, <https://doi.org/10.1029/2018GL080544>, 2019.

834 Zender, C. S., Bian, H., and Newman, D.: Mineral Dust Entrainment and Deposition (DEAD) model:
835 Description and 1990s dust climatology, *J. Geophys. Res.*, 108, 4416,
836 <https://doi.org/10.1029/2002JD002775>, 2003a.

837 Zender, C. S., Newman, D., and Torres, O.: Spatial heterogeneity in aeolian erodibility: Uniform, topographic,
838 geomorphic, and hydrologic hypotheses, *J. Geophys. Res.*, 108, 4543,
839 <https://doi.org/10.1029/2002JD003039>, 2003b.

840 Zhang, J., Reid, J. S., and Holben, B. N.: An analysis of potential cloud artifacts in MODIS over ocean aerosol



841 optical thickness products, *Geophys. Res. Lett.*, 32, L15803, <https://doi.org/10.1029/2005GL023254>, 2005.

842 Zhang, L., Li, Q. B., Gu, Y., Liou, K. N., and Meland, B.: Dust vertical profile impact on global radiative

843 forcing estimation using a coupled chemical-transport–radiative-transfer model, *Atmos. Chem. Phys.*, 13,

844 7097-7114, <https://doi.org/10.5194/acp-13-7097-2013>, 2013.

845

846

847

848

849

850

851

852

853

854

855

856

857

858

859

860

861

862



863 **Tables**

864 **Table 1.** Description of the models on their dust physical characteristics.

	Resolution	Aerosol Module	Geometric Standard Deviations	Mass Fraction of Dust Emission (%)	Dust Emission Scheme
CESM1	1°, 30L	MAM4 (Liu et al., 2016) (3 modes, 0.01-0.1-1.0-10.0 µm)	1.6, 1.8, 1.8	0.00165, 1.1, 98.9 (Kok, 2011)	Zender et al. (2003a)
CESM2	1°, 32L	MAM4 (Liu et al., 2016) (3 modes, 0.01-0.1-1.0-10.0 µm)	1.6, 1.6, 1.2	0.00165, 1.1, 98.9 (Kok, 2011)	Zender et al. (2003a)
E3SMv1	1°, 72L	MAM4 (Liu et al., 2016) (2 modes, 0.1-1.0-10.0 µm)	1.8, 1.8	3.2, 96.8 (Zender et al., 2003a)	Zender et al. (2003a)
MERRA-2	0.5°, 72L	GOCART (Chin et al., 2002) (5 bins, 0.2-2.0-3.6-6.0-12.0-20.0 µm)		6.6, 20.6, 22.8, 24.5, 25.4 (Ginoux et al., 2001)	Ginoux et al. (2001)

865

866

867

868

869

870

871

872

873

874

875

876

877

878

879



880 **Table 2.** Global annual mean dust mass budgets, DOD, and MEE

	CESM1	CESM2	E3SMv1	MERRA-2
Emission (Tg yr ⁻¹)	3868 (43, 3826)	1820 (20, 1800)	3399 (109, 3291)	1636 (1220)
Dry deposition (Tg yr ⁻¹)	2496 (7, 2489)	675 (5, 670)	2638 (29, 2609)	1168 (750)
Wet deposition (Tg yr ⁻¹)	1379 (36, 1343)	1151 (15, 1136)	764 (80, 684)	880 (865)
Burden (Tg)	24.7 (0.7, 24.0)	19.5 (0.3, 19.2)	17.9 (2.0, 15.9)	23.5 (22.8)
Lifetime (day)	2.33 (5.92, 2.29)	3.90 (5.91, 3.88)	1.92 (6.84, 1.76)	4.19 (5.17)
DOD	0.0219	0.0212	0.0238	0.0312
MEE (m ² g ⁻¹)	0.452	0.553	0.677	0.677

881 Note: the values in parentheses for CESM1, CESM2, and E3SMv1 correspond to the accumulation mode
882 (0.1-1 μm) and coarse mode (1-10 μm), respectively; the values in parentheses for MERRA-2 correspond to
883 bins 1-4 (0.2-12.0 μm)

884

885

886

887

888

889

890

891

892

893

894

895

896

897



898 **Table 3.** Global seasonal mean DOD (60°S-60°N)

	MAM	JJA	SON	DJF
CESM1	0.0314 (0.0956, 0.0083)	0.0286 (0.0774, 0.0111)	0.0184 (0.0553, 0.0051)	0.0156 (0.0445, 0.0052)
CESM2	0.0253 (0.0722, 0.0083)	0.0208 (0.0534, 0.0090)	0.0218 (0.0571, 0.0090)	0.0186 (0.0464, 0.0085)
E3SMv1	0.0293 (0.0808, 0.0106)	0.0281 (0.0713, 0.0125)	0.0194 (0.0529, 0.0073)	0.0162 (0.0420, 0.0069)
MERRA-2	0.0465 (0.1095, 0.0236)	0.0369 (0.0853, 0.0196)	0.0232 (0.0559, 0.0113)	0.0221 (0.0501, 0.0119)
CALIOP L15	0.0332 (0.0799, 0.0170)	0.0339 (0.0765, 0.0192)	0.0183 (0.0460, 0.0087)	0.0173 (0.0407, 0.0092)
CALIOP Y15	0.0385 (0.0864, 0.0217)	0.0366 (0.0769, 0.0222)	0.0248 (0.0523, 0.0150)	0.0231 (0.0437, 0.0160)
MODIS Terra	0.0788 (0.1333, 0.0595)	0.0780 (0.1269, 0.0615)	0.0623 (0.0937, 0.0511)	0.0607 (0.0953, 0.0504)
MODIS Aqua	0.0706 (0.1209, 0.0529)	0.0707 (0.1144, 0.0560)	0.0522 (0.0813, 0.0419)	0.0569 (0.0918, 0.0464)
MISR	(, 0.0413)	(, 0.0406)	(, 0.0351)	(, 0.0328)

899 Note: the values in parentheses are for land and ocean, respectively.

900

901

902

903

904

905

906

907

908

909

910

911

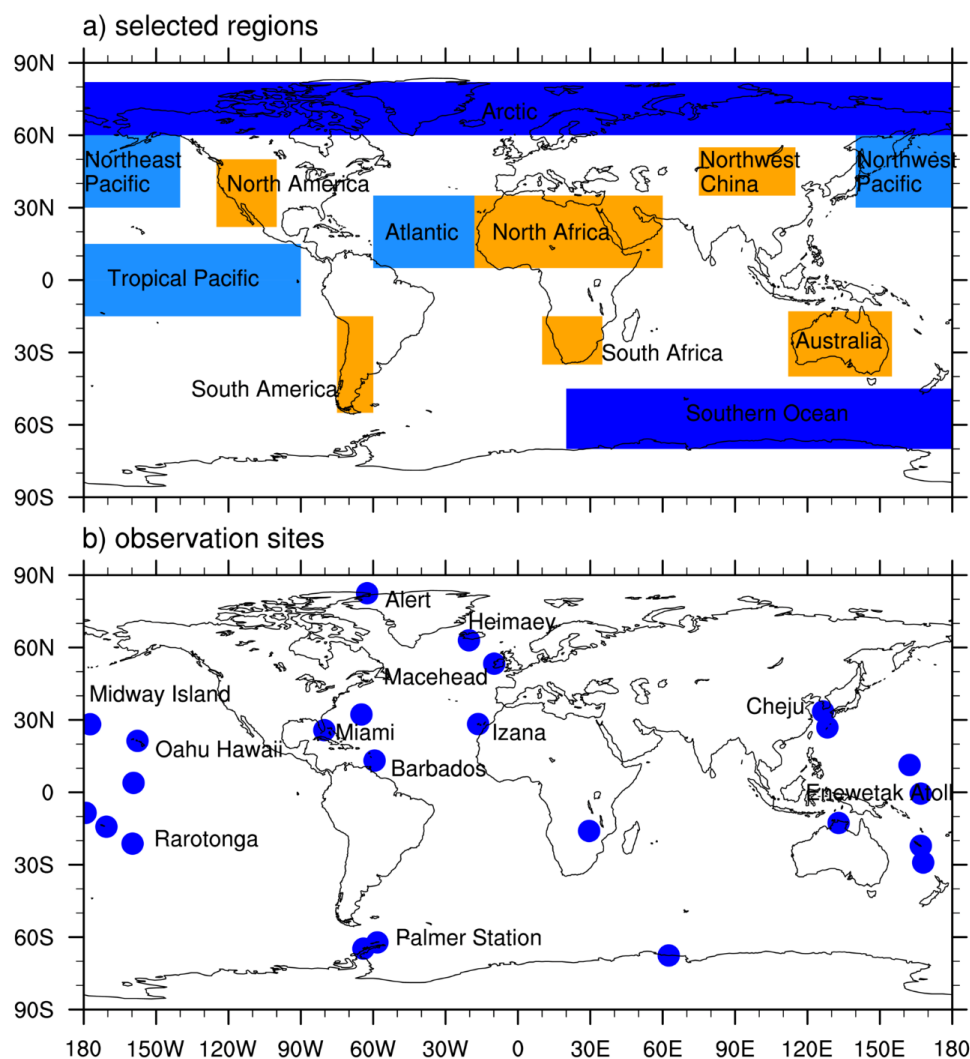
912

913

914



915 **Figures**



916

917 **Figure 1.** Illustration of (a) 12 selected domains and (b) network of stations measuring dust surface

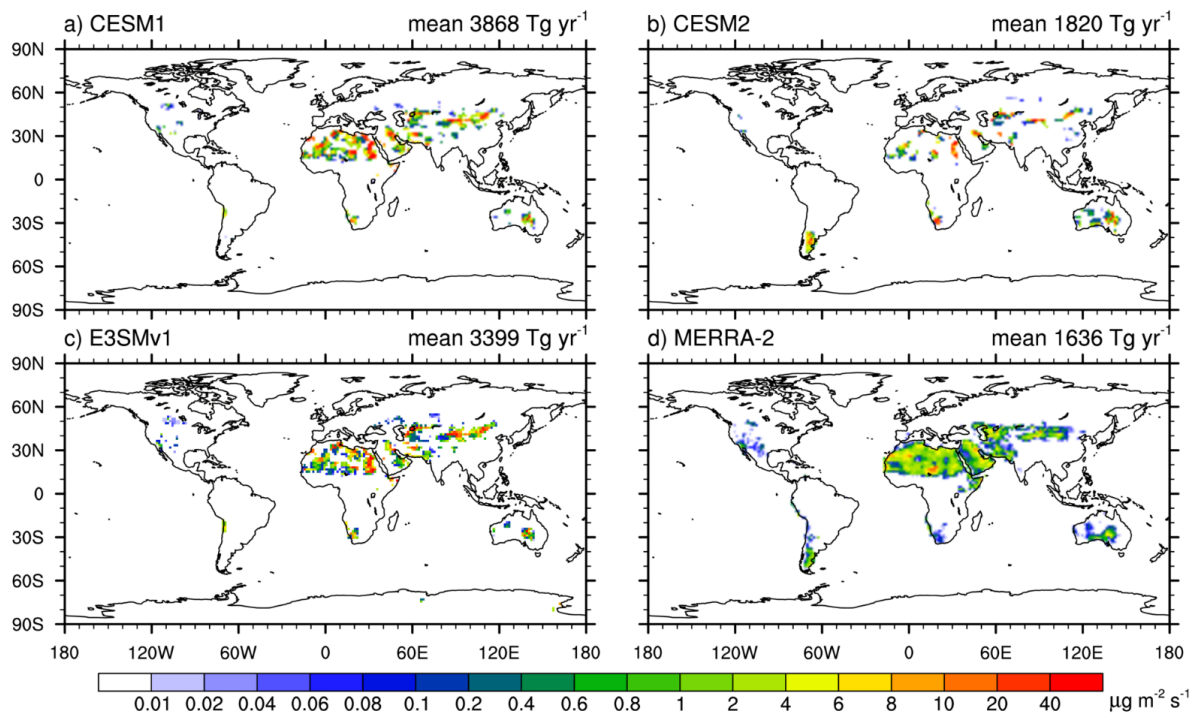
918 concentrations.

919

920

921

922



923

924 **Figure 2.** Spatial distributions of global annual mean dust emission ($\mu\text{g m}^{-2} \text{s}^{-1}$) from model experiments.

925 The values are global annual mean dust emission.

926

927

928

929

930

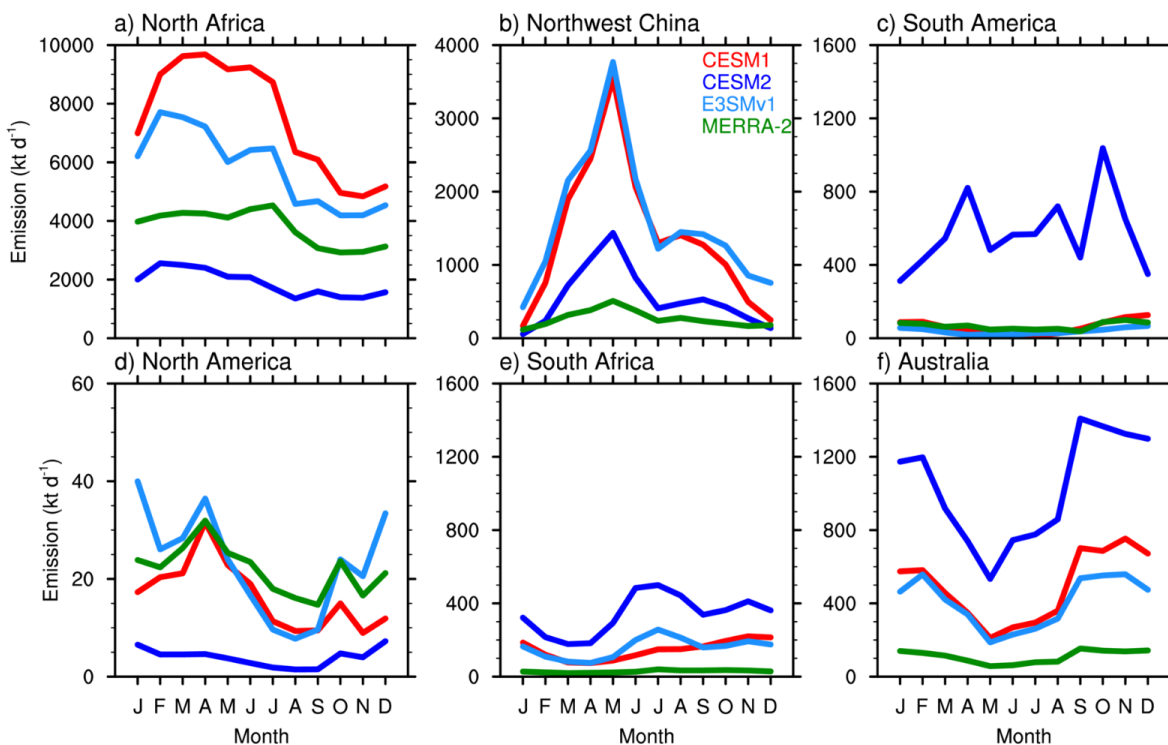
931

932

933

934

935



936

937 **Figure 3.** Seasonal variations of dust emission (kt d^{-1}) in source regions: (a) North Africa, (b) Northwest

938 China, (c) South America, (d) North America, (e) South Africa, and (f) Australia.

939

940

941

942

943

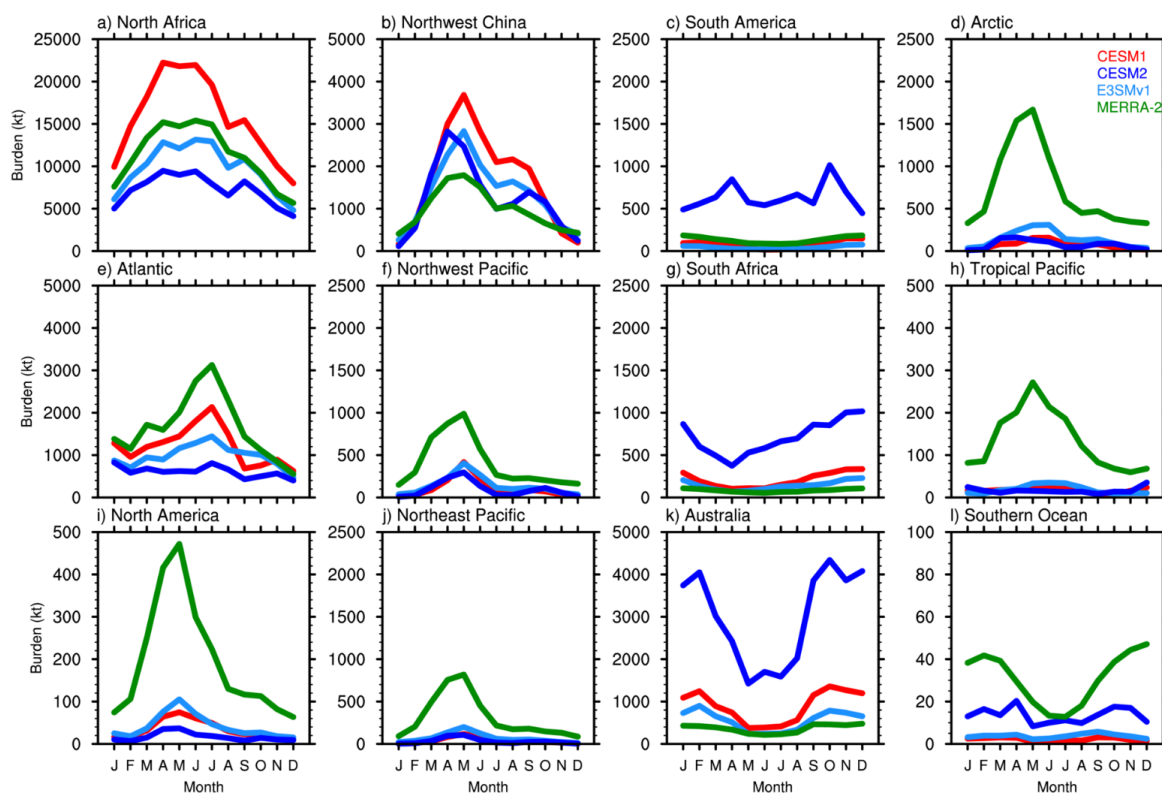
944

945

946

947

948



949

950 **Figure 4.** Seasonal variations of dust burden (kt) from model experiments over 12 selected regions during
951 2007-2009.

952

953

954

955

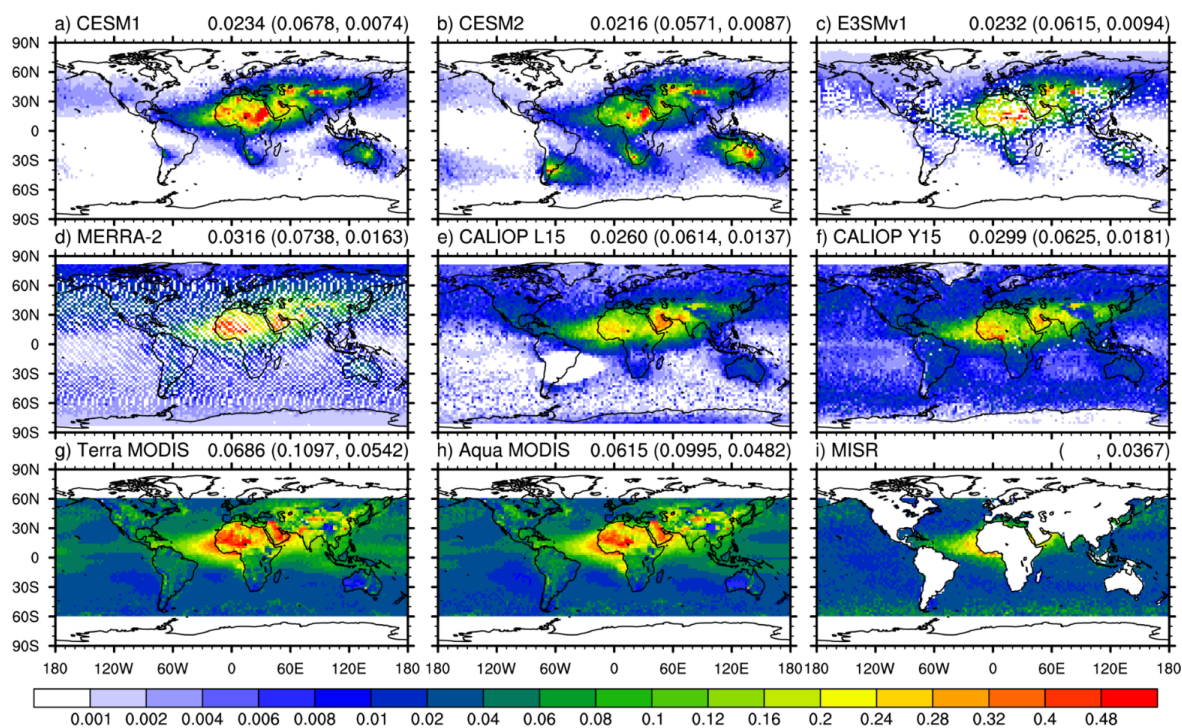
956

957

958

959

960



961

962 **Figure 5.** Spatial distributions of global annual mean DOD from model experiments, CALIOP, MODIS, and
963 MISR during 2007-2009. The values are annual mean DOD between 60°S and 60°N. The values in the
964 parentheses are annual mean DOD over land and ocean, respectively. The stripe pattern of white space in (c)
965 and (d) is due to the date collocation.

966

967

968

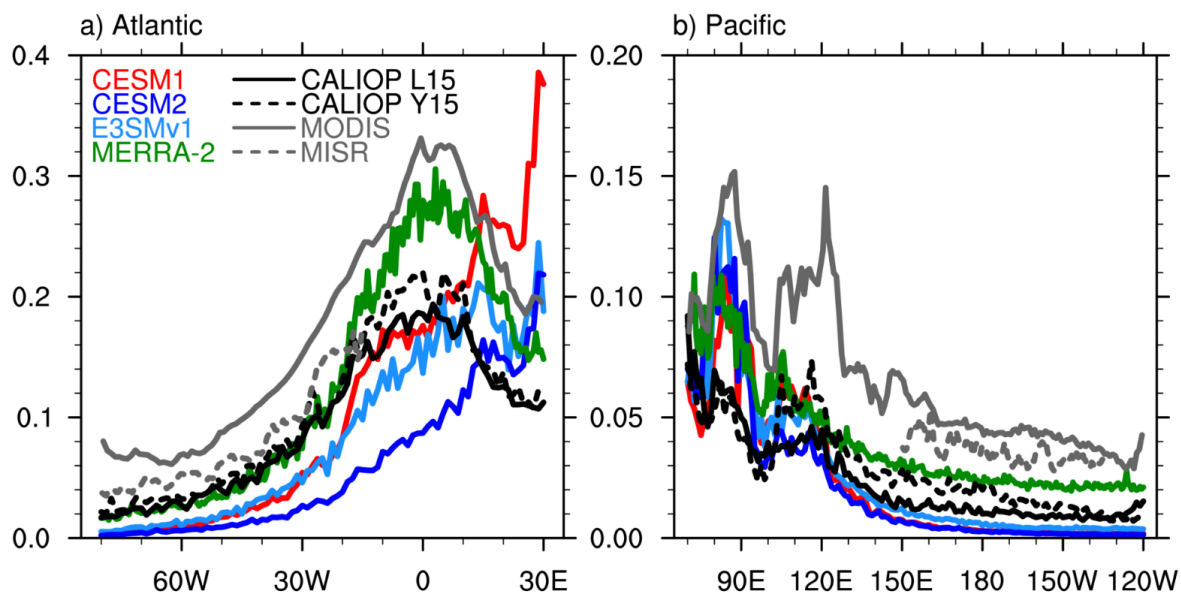
969

970

971

972

973



974

975 **Figure 6.** Meridional mean of DOD from model experiments, CALIOP, MODIS, and MISR across the (a)

976 Atlantic (0°-35°N) and (b) Pacific (30°N-60°N).

977

978

979

980

981

982

983

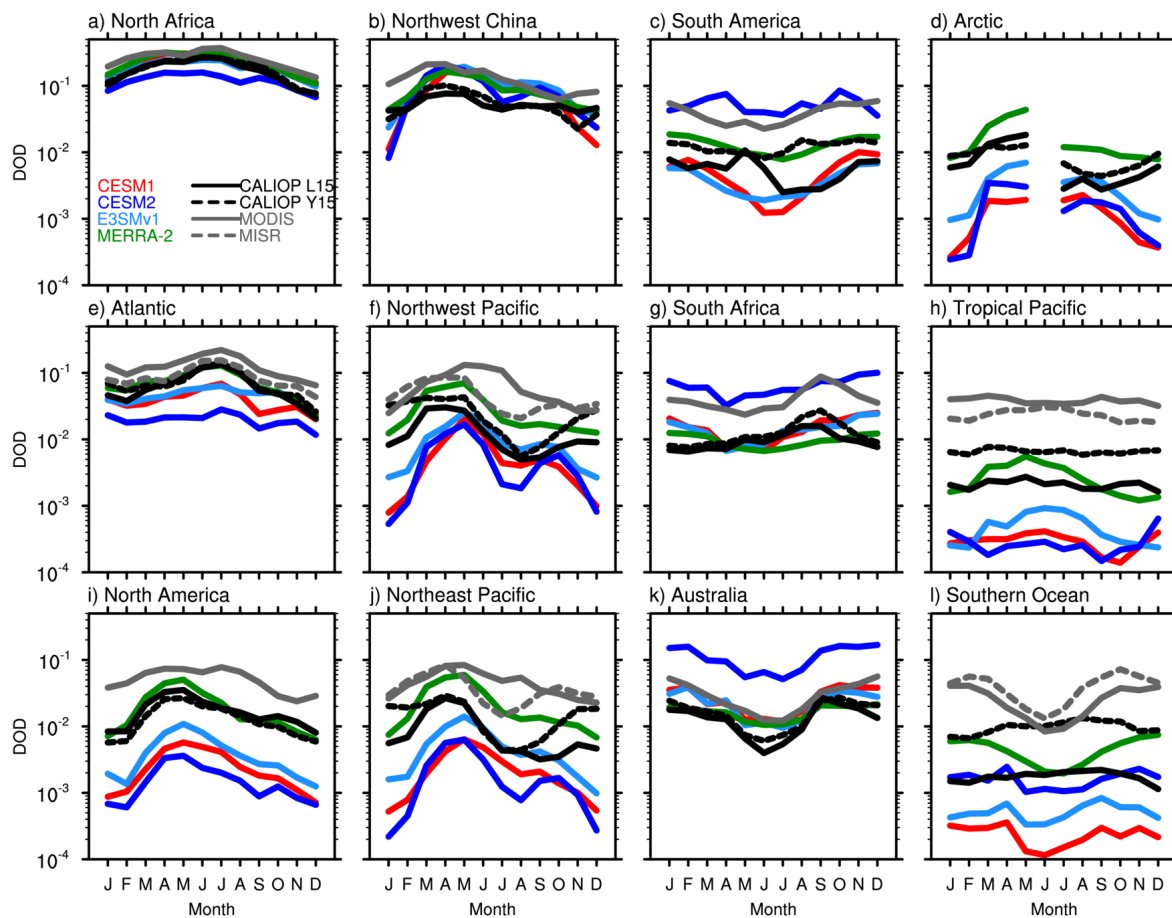
984

985

986

987

988



989

990 **Figure 7.** Seasonal variations of DOD from model experiments, CALIOP, MODIS, and MISR over 12

991 selected regions during 2007-2009. The gap in (d) is due to the missing of nighttime data during the polar

992 day.

993

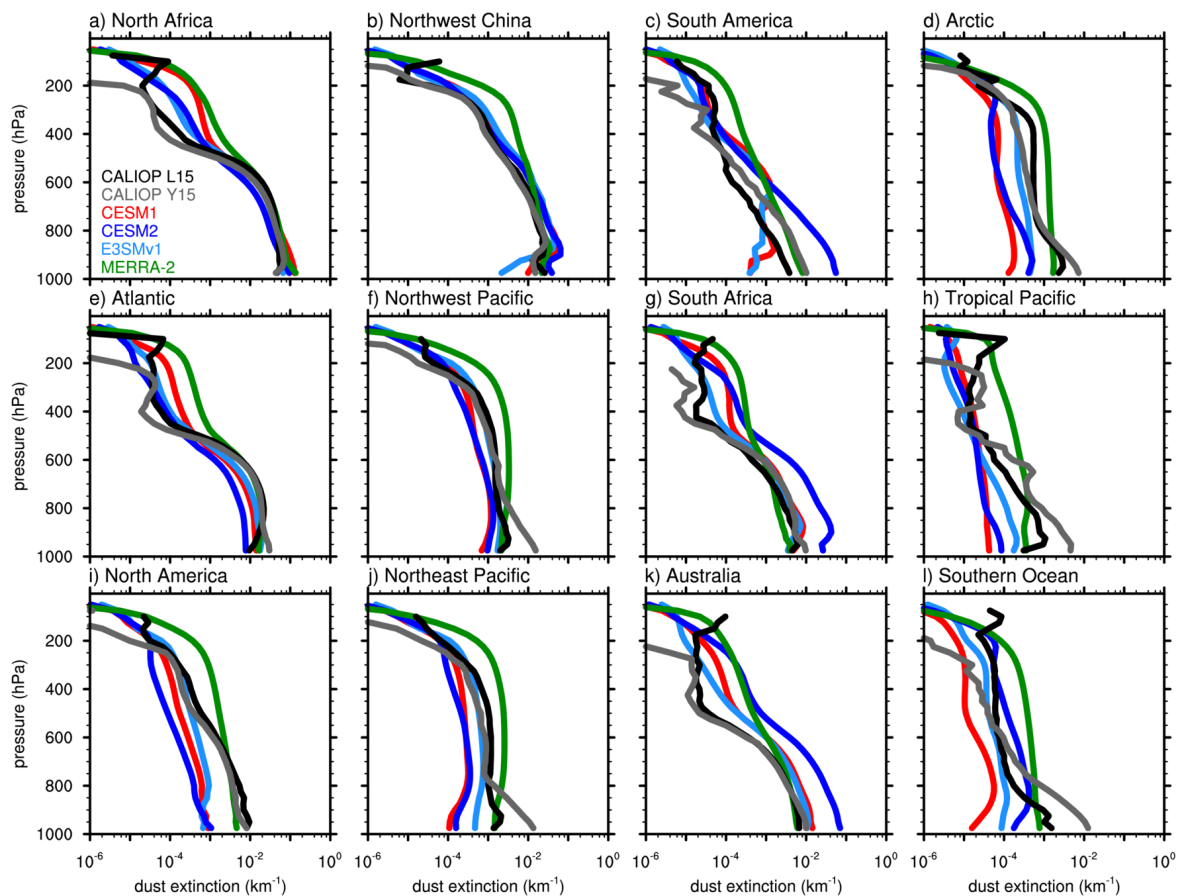
994

995

996

997

998



999

000 **Figure 8.** Vertical profiles of annual mean dust extinction (km^{-1}) from model simulations and CALIOP over

001 12 selected regions during 2007-2009.

002

003

004

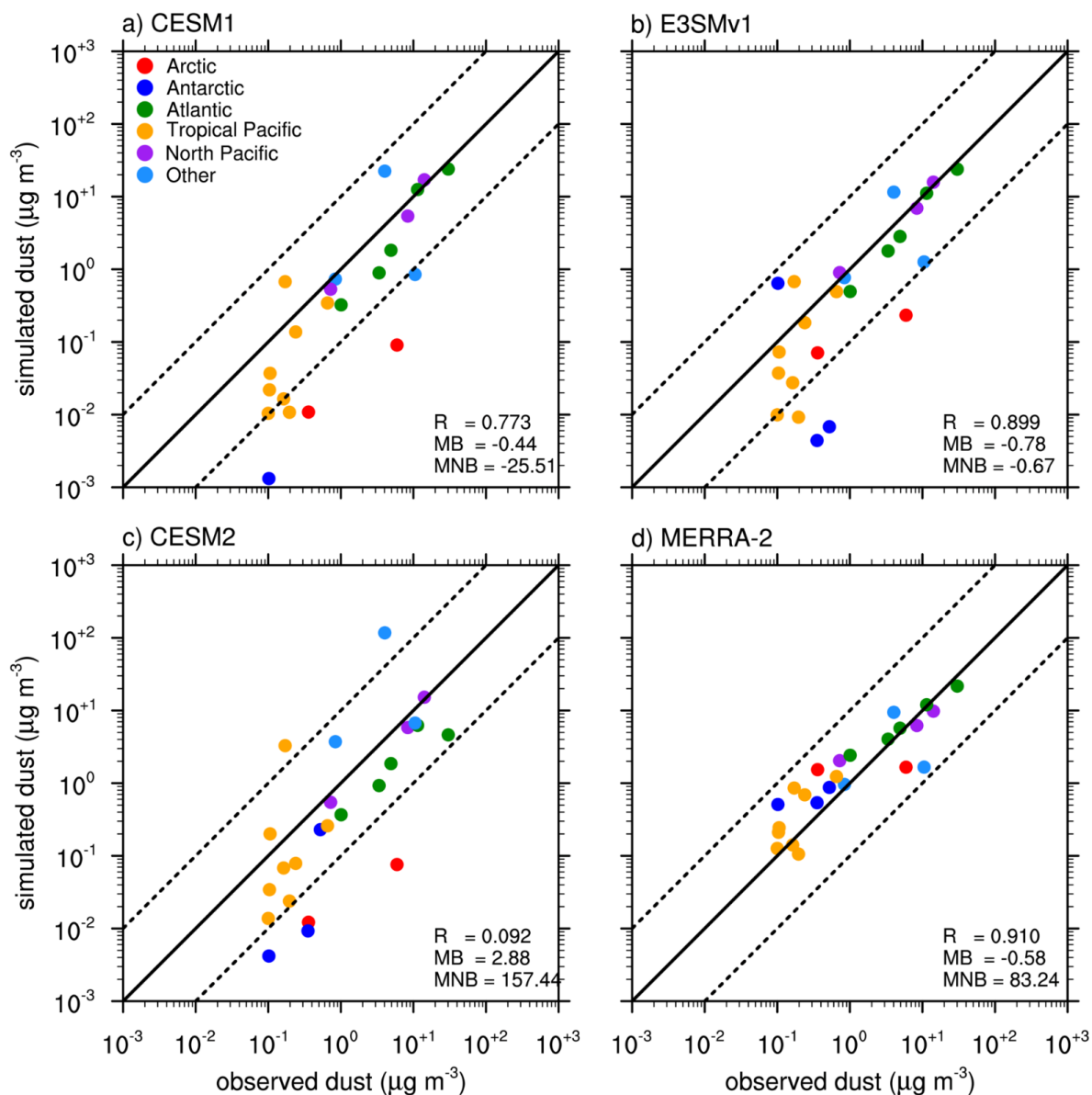
005

006

007

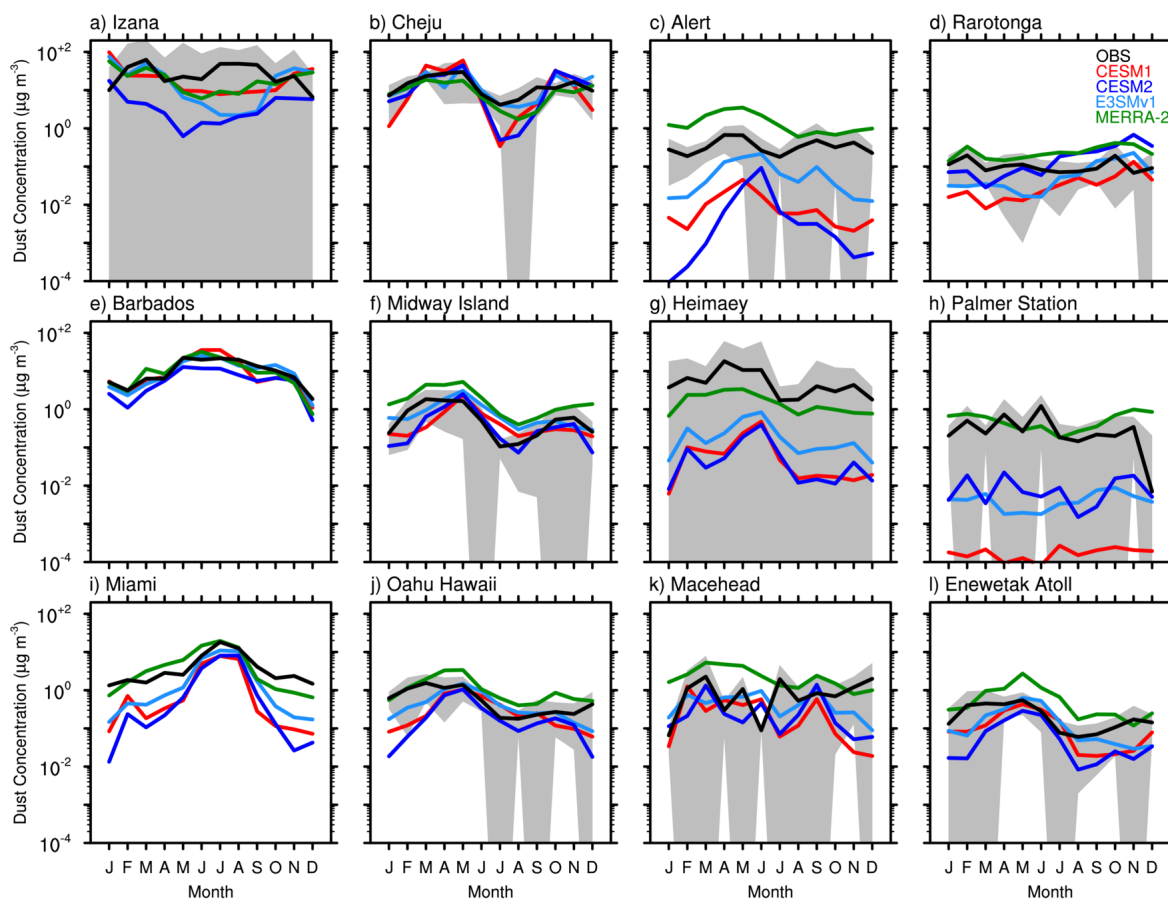
008

009



.010

.011 **Figure 9.** Observed and simulated annual mean dust surface concentrations ($\mu\text{g m}^{-3}$) at 24 sites. The
 .012 measurements at Alert are from Fan (2013); the observations at Heimaey, Barbados, and Miami are from
 .013 Prospero et al. (2012); the dataset for the other 20 sites are from Huneus et al. (2011). These sites were
 .014 operated by the University of Miami (Arimoto et al., 1996; Prospero et al., 1989, 1996). Different color
 .015 represents different regions.



.016

.017 **Figure 10.** Seasonal variations of dust surface concentrations ($\mu\text{g m}^{-3}$) from model simulations and ground

.018 measurements at 12 selected sites. Shaded areas are for plus/minus one standard deviation of observations.

.019

.020

.021

.022

.023

.024

.025